# **Inorganic Chemistry**

pubs.acs.org/IC Article

# Trivalent Cations Slow Electron Transfer to Macrocyclic Heterobimetallic Complexes

Joseph P. Karnes, Amit Kumar, Julie A. Hopkins Leseberg, Victor W. Day, and James D. Blakemore\*



Cite This: Inorg. Chem. 2024, 63, 8710-8729



**ACCESS** I

III Metrics & More

Article Recommendations

Supporting Information

**ABSTRACT:** Incorporation of secondary redox-inactive cations into heterobimetallic complexes is an attractive strategy for modulation of metal-centered redox chemistry, but quantification of the consequences of incorporating strongly Lewis acidic trivalent cations has received little attention. Here, a family of seven heterobimetallic complexes that pair a redox-active nickel center with La<sup>3+</sup>, Y<sup>3+</sup>, Lu<sup>3+</sup>, Sr<sup>2+</sup>, Ca<sup>2+</sup>, K<sup>+</sup>, and Na<sup>+</sup> (in the form of their triflate salts) have been prepared on a heteroditopic ligand platform to understand how chemical behavior varies across the comprehensive series. Structural data from X-ray diffraction analysis demonstrate that the positions adopted by the secondary cations in the crown-ether-like site of the ligand relative to nickel are dependent primarily on the secondary cations' ionic radii and

Mapping Steric Crowding in Nickel Microenvironments

Comprehensive X-ray diffraction analysis

Tunable electron transfer rate

Free volume analysis with SambVca

that the triflate counteranions are bound to the cations in all cases. Electrochemical data, in concert with electron paramagnetic resonance studies, show that nickel(II)/nickel(I) redox is modulated by the secondary metals; the heterogeneous electron-transfer rate is diminished for the derivatives incorporating trivalent metals, an effect that is dependent on steric crowding about the nickel metal center and that was quantified here with a topographical free-volume analysis. As related analyses carried out here on previously reported systems bear out similar relationships, we conclude that the placement and identity of both the secondary metal cations and their associated counteranions can afford unique changes in the (electro)chemical behavior of heterobimetallic species.

# **■ INTRODUCTION**

Gaining control over the electron-transfer (ET) behaviors of redox-active molecules and materials is among the chief design challenges faced by synthetic inorganic chemists. The requirement to control redox chemistry, or at least reliably influence it, impacts the development of molecular catalysts, 1,2 study of small-molecule activation, 3,4 and efforts to observe the chemical properties of molecules featuring elements in uncommon oxidation states.<sup>5-7</sup> In each of these cases, understanding how the environment (coordination, solvation, etc.) of a given redox-active metal can be modified to result in desirable redox properties is critical. Significant efforts are underway in a variety of fields to molecularly engineer the key features of ET, including reduction potentials and ET rates. This broad interest is no doubt attributable to the numerous advantages that can come from favoring desirable redox reactions while disfavoring others, including increased selectivity in catalysis, increased efficiency in ET-dependent energy conversion systems, and improved yields during interconversion of oxidation states.

Incorporation of electropositive metal cations into complexes containing redox-active metal centers is a proven strategy for accessing chemical behaviors that are distinctive from those displayed by the analogous monometallic precursor complexes. In this realm, divergent synthetic protocols are

most attractive, enabling access to families of complexes built from monometallic precursors that feature one or more binding sites for incorporation of secondary metal cations. A study of such complexes has shown that chemical properties such as reduction potentials, 3,8-10 energies of electronic absorption transitions, energies of bond vibrations, 10 catalytic abilities, 2,3,11 and even magnetic behaviors 12 can be systematically tuned based on the identity of the incorporated secondary metal cations. Recently, we have gathered evidence for the hypothesis that, in cases where bridging ligands are present between redox-active metals and the incorporated secondary electropositive metal cations, there is an induced diminishment of the donor power of the bridging ligands that depends on the identity of the secondary cation.<sup>10</sup> Other frameworks for understanding the origin of tuning effects have also been developed, including the concepts of cation-induced electric fields, 13,14 cation-driven structural deformations, 15 and size-

Received: January 18, 2024 Revised: April 11, 2024 Accepted: April 15, 2024 Published: April 26, 2024





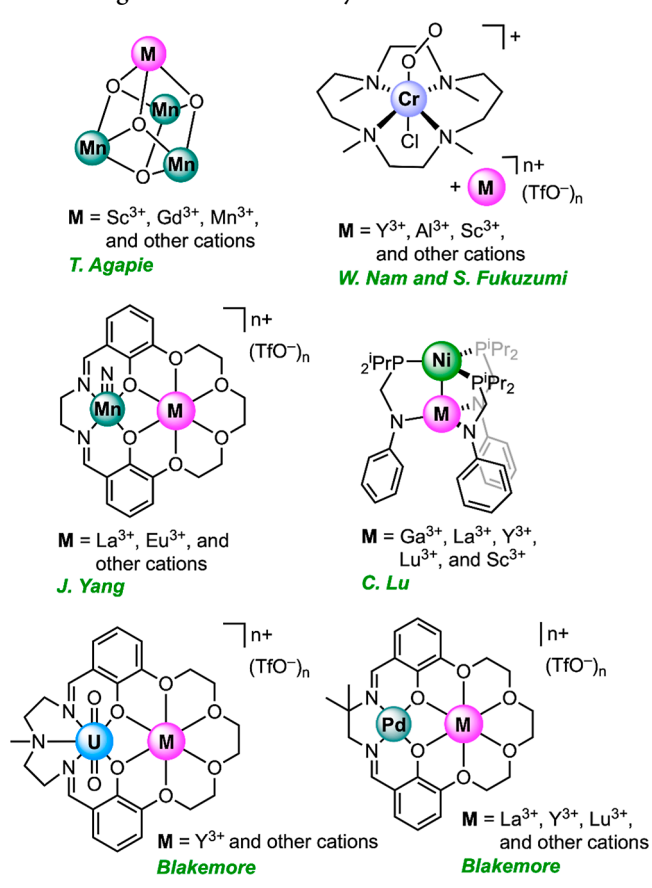
dependent behaviors.<sup>2</sup> Regardless of the interpretation around their origins, the use of cations to modulate redox chemistry is currently attracting significant attention as this strategy appears broadly useful.

The electropositive metal cations that are commonly used for tuning purposes span a range of charges, sizes, and coordination numbers and often include mono- and divalent cations such as K<sup>+</sup>, Na<sup>+</sup>, Ba<sup>2+</sup>, and Ca<sup>2+</sup>. Trivalent cations such as Sc3+ attract special attention, however, as the effects that they promote are typically more significant than those induced by mono- and divalent cations. Generally speaking, this observation is related to demonstrations that electropositive metal cations, in effect, function as Lewis acids in most applications where they are incorporated into complexes to modulate redox chemistry. To rationalize cation-driven tuning effects on a unified and rather intuitive scale, Brønsted-Lowry acidity data for metal-aqua complexes are often used, as gathered together by Perrin in an important and comprehensive catalogue. 16 The scale on which metal cations can be compared uses the  $pK_a$  values of water bound to metal-aqua complexes of the metal cations of interest to parameterize their effect(s) on multimetallic complexes. This approach to describing tunable behaviors in heterobimetallic complexes, and larger systems, has proven robust across solvent systems. 17,18 The robustness of the scale likely derives from the observation that the experimental  $pK_a$  values shift reliably based on charge density, 19 taking into account both charge and ionic radius.20

Since beginning work in the area of heterobimetallic chemistry, we have noted a trend in the field: the properties of complexes containing a redox-active metal and a trivalent metal cation serving as a tuning agent often display properties that are the most dramatically shifted in any comparison series (see Chart 1). Foundational work from Agapie and co-workers showed that trivalent rare-earth cations could be used to induce greatly shifted reduction potentials in manganese and iron clusters.<sup>3</sup> We showed later that Nd<sup>3+</sup> and Y<sup>3+</sup> could be used as desired for tuning of redox-active nickel complexes, although derivatives containing these cations showed solventdependent stabilities in contrast to analogues incorporating mono- or divalent secondary cations.<sup>5</sup> Nam and Fukuzumi have used Sc<sup>3+</sup> and other trivalent cations to promote reactivity of oxygen-derived species,<sup>4</sup> although the heterobimetallic species in these cases were assembled in situ to form the activated system.<sup>22</sup> A unifying theme of all these reports is that the high effective Lewis acidity of the trivalent cations appears to grant them a privileged position as drivers of significant and potentially useful changes in the chemical properties of redoxactive metal complexes.

However, few studies have examined the ET kinetics of heterobimetallic complexes and how these kinetics may depend on the identity of the incorporated secondary metal cations. On the one hand, ET kinetics are critical in redoxinduced turnover and the time-dependent yield of reduced/oxidized products, impacting efficiency and selectivity considerations in inorganic/organometallic systems. On the other hand, numerous studies have examined the tuning of thermodynamic reduction potentials by incorporation of secondary, Lewis acidic metal cations into heterobimetallic complexes while neglecting the interrelated kinetic considerations. We anticipated that investigation of the tuning of ET kinetics by secondary metal cations would be enhanced, however, by comprehensive structural studies on the redox-

Chart 1. Examples of Tunable Heterobimetallic Complexes Containing Trivalent Secondary Cations



active complexes chosen for investigation. In particular, we anticipated that study of a family of derivatives featuring mono-, di-, and trivalent secondary cations would be attractive because the consequences of incorporating the important trivalent cations could be compared to those incorporating mono- and divalent cations in a systematic fashion.

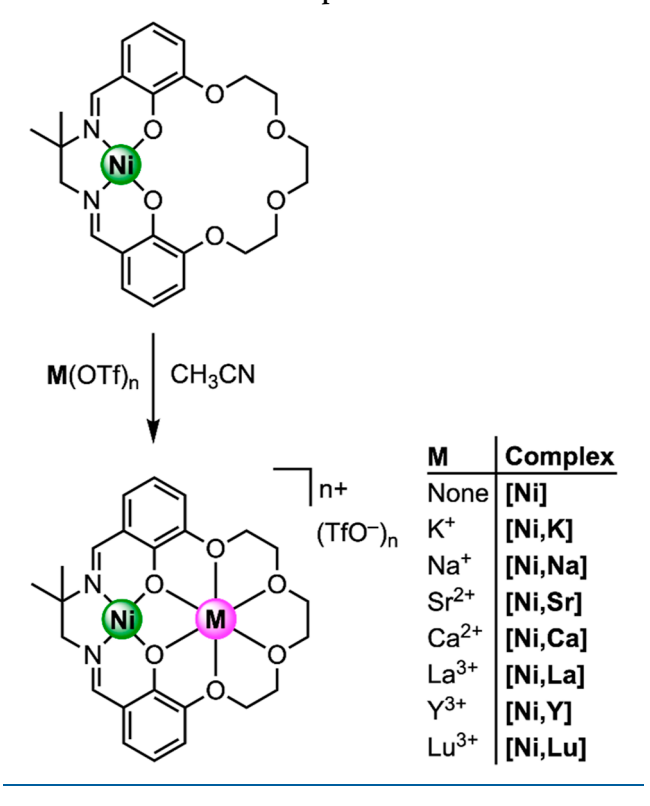
Here, we report the synthesis, isolation, and study of a collection of heterobimetallic nickel complexes built upon a Reinhoudt-type ligand framework that enable quantification of the influence of secondary metal cations on nickel(II)/ nickel(I) redox chemistry. Incorporation of a broad range of metal cations (La<sup>3+</sup>, Y<sup>3+</sup>, Lu<sup>3+</sup>, Sr<sup>2+</sup>, Ca<sup>2+</sup>, K<sup>+</sup>, and Na<sup>+</sup>) was carried out, and single-crystal X-ray diffraction (XRD) data confirmed the assembly of homologous  $[Ni^{II}(\mu_2-O_{phenoxide})-$ M<sup>n+</sup>] cores in all cases except that of the derivative featuring Y<sup>3+</sup> (which resisted crystallization), providing a comprehensive series of complexes upon which to base an investigation of the role of the secondary metal cations in influencing the properties of the heterobimetallic species. The XRD studies reveal that the position adopted by the secondary metal cations is dependent on their ionic radii and that the triflate counteranions associated with the secondary cations are bound inner sphere in all cases, resulting in steric crowding about the redox-active nickel centers. This steric crowding impacts the heterogeneous ET kinetics associated with redox cycling, an effect that was quantified through a topographical buried volume analysis. As these observations suggest that trivalent cations and their counteranions can directly impact tunable behaviors, this report identifies key structural design

elements that can be used to influence the kinetics of ET behavior in multimetallic systems.

## RESULTS

**Synthesis and Characterization.** Our group prefers to use a divergent synthetic strategy for the preparation of heterobimetallic complexes, and we have found that preparation of suitable monometallic precursor complexes can enable rapid access to derivatives featuring incorporated secondary metal cations. Here, we turned to a monometallic nickel(II) complex, denoted as [Ni], that was previously synthesized by Reinhoudt and co-workers.<sup>23,24</sup> [Ni] features a Schiff-base binding site for nickel as well as an appended crown-ether-like site for binding secondary cations (see Scheme 1). The ligand

Scheme 1. Divergent Synthetic Strategy for Heterobimetallic Nickel Complexes



supporting the monometallic complex is quite useful (denoted here as L<sub>salmen</sub>), as it is based on a 1,1-dimethyl-1,2ethylenediamine-containing backbone that favors macrocyclization via the Thorpe-Ingold effect.<sup>25</sup> The favorability of the macrocyclization reaction enables isolation of [Ni] and subsequent use of this precursor for the divergent metalation that can yield the heterobimetallic complexes developed for study. We note here that this approach differs from a prior study<sup>14</sup> that utilized convergent metalation to produce heterobimetallic complexes of nickel with mono- and divalent secondary metal cations; in that study, the utilization of simpler ethylenediamine as the ligand backbone appears to preclude the study of adducts with trivalent cations. We prepared [Ni] as described by Reinhoudt and co-workers; the <sup>1</sup>H NMR spectrum of the isolated material matched well with results obtained in the prior work (see Figure S1).<sup>23</sup>

With [Ni] in hand, heterobimetallic complexes of form [Ni,M] could be prepared by reaction of the monometallic

starting material with the corresponding metal triflate salts. Specifically, 1 equiv of metal triflate salt was reacted with [Ni] to obtain 1:1 bimetallic complexes in high yields in all cases (95-98%; see the Experimental Section). As in our previous work, we used the  $pK_a$  values of the metal—aqua complexes of the incorporated metal cations to describe their effective Lewis acidities; the work here spans from the weakly acidic  $K^+$  (p $K_2$  = 16.0) to strongly acidic Lu<sup>3+</sup> (7.9). <sup>16</sup> <sup>1</sup>H, <sup>13</sup>C{<sup>1</sup>H}, and <sup>19</sup>F NMR studies (see Figures S5-S39), as well as elemental analyses of all the isolated complexes, were performed successfully, validating the clean formation of the targeted complexes. As we found in prior work with palladium(II) complexes based on L<sub>salmen</sub>, the downfield resonances corresponding to the imine protons of each complex are particularly diagnostic of coordination of the redox-inactive metal cations; more significant downfield shifts are associated with the derivatives containing the more strongly Lewis acidic cations (see Figure S35 which shows the case of [Ni,Lu]). Additionally, no evidence was obtained for scrambling of the metal cations between the two sites of  $L_{salmen}$ ; this ligand can be concluded to effectively support orthogonal metalation.

Single-Crystal XRD Analysis. XRD analysis of the heterobimetallic complexes confirmed the assembly of the desired  $[Ni^{II}(\mu_2-O_{phenoxide})M^{n+}]$  cores in each case (see Figure 1). See Table 1 for the metrical data obtained from the XRD analysis and pp. S59-S79 for details on each structure. In each case, the secondary metal cation is bound in the crown-etherlike site as expected. Within the pairs of structures that feature secondary cations having the same charge, the formal coordination numbers (CN values) are in accord with the ions' relative sizes. K+ adopts CN = 9 (see p. \$59-\$60 for details on this determination) and features a bound triflate, while smaller Na<sup>+</sup> adopts CN = 7 and features a  $\kappa^1$ -triflate; similarly,  $Sr^{2+}$  adopts CN = 9 and features one  $\kappa^{1}$ -triflate and one  $\kappa^2$ -triflate, while smaller Ca<sup>2+</sup> adopts CN = 8 with two  $\kappa^1$ triflates. The trivalent cations La3+ and Lu3+ show similar behaviors, with all three of their accompanying triflate counteranions bound in all cases; La<sup>3+</sup> features CN = 10 with one  $\kappa^2$ -triflate and Lu<sup>3+</sup> features CN = 9 with three  $\kappa^1$ triflates. Considering all this data, we conclude that the size of the secondary cations, which can be parameterized through their Shannon ionic radii (see Table 1), influences their coordination behavior within  $L_{salmen}$ .

In the solid-state structures of all the heterobimetallic complexes except that of [Ni,K], the metal-containing complexes do not appear to interact in any significant fashion with each other and display only minimal, noncovalent packing interactions with neighboring species. However, [Ni,K] appears to form a weakly bonded dimeric unit in the solid state that is composed of 2 equiv of the targeted heterobimetallic complex (see Figure S96). These 2 equiv of the as-synthesized [Ni,K] interact across a crystallographic inversion center; only a single set of atom positions for [Ni,K] are defined in the asymmetric unit, but inspection of the environment of [Ni,K] reveals pairwise interactions between individual heterobimetallic complexes. The result is a pair of nickel coordination planes slipped to produce a [Ni<sub>2</sub>,O<sub>2</sub>] parallelogram with "axial" Ni···O<sub>phen</sub> distances of 3.57 Å and similarly long Ni···Ni separations of 3.63 Å. On the one hand, a search of the Cambridge Structural Database<sup>26</sup> for nickel salen or salophen complexes interacting with "axial" oxygen ligands in an intramolecular, bonded fashion revealed Ni···O distances spanning the range from 1.79 to 2.41 Å.27-30 On the other

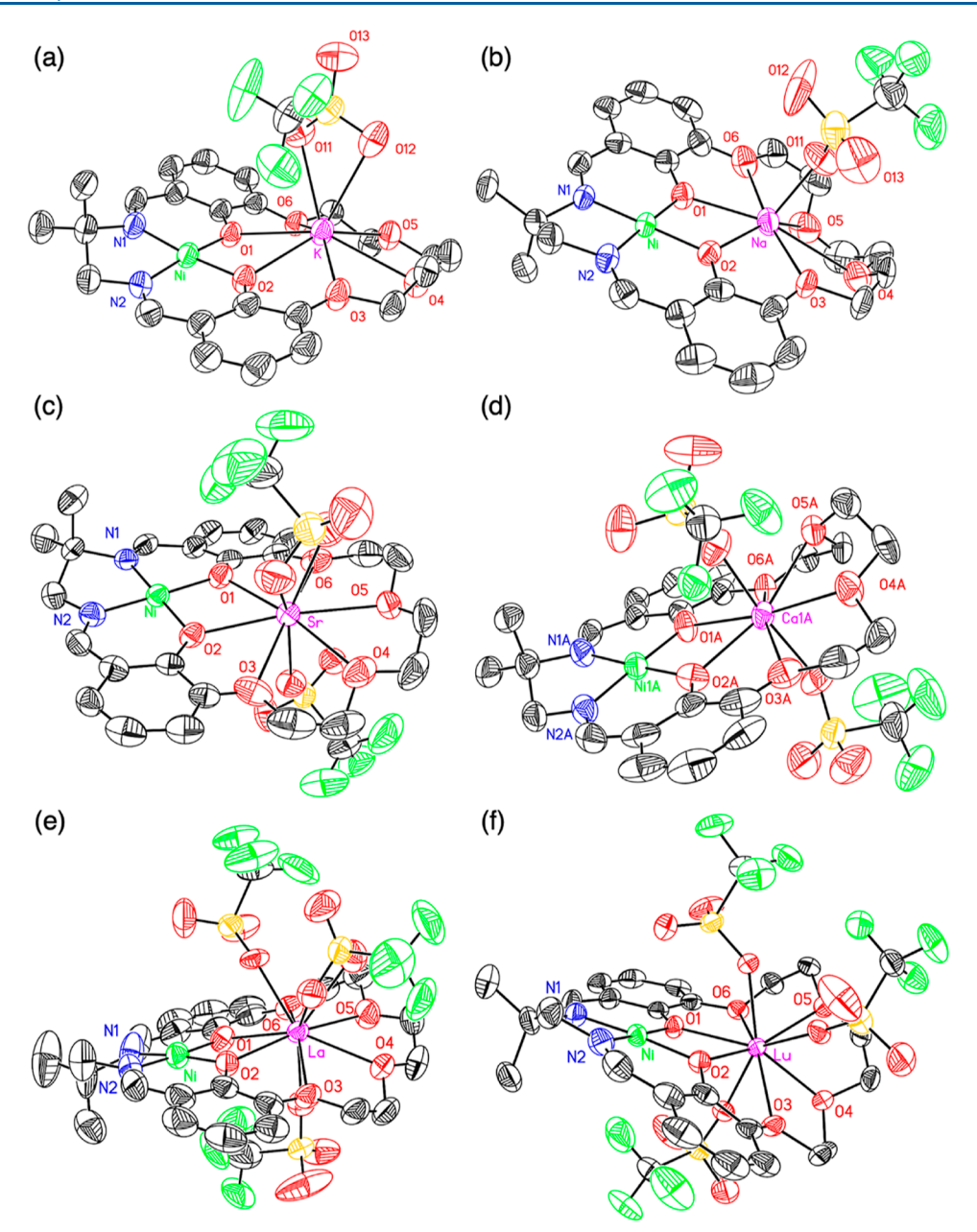


Figure 1. Solid-state structures (XRD) of the heterobimetallic complexes featuring mono-, di-, and trivalent cations. (a) K<sup>+</sup> adduct; (b) Na<sup>+</sup> adduct; (c) Sr<sup>2+</sup> adduct; (d) Ca<sup>2+</sup> adduct; (e) La<sup>3+</sup> adduct; and (f) Lu<sup>3+</sup> adduct. All hydrogen atoms, outer-sphere cocrystallized solvent, and atoms associated with minor components of structural disorder are omitted for clarity. Displacement ellipsoids are shown at the 50% probability level.

hand, a search of the CSD for intermolecular Ni···O contacts revealed a span of 2.68–3.15 Å; as the Ni···O in our complex is longer than these prior examples at 3.57 Å, the association between heterobimetallic complexes can be concluded to be rather weak. Additionally, we note that inspection of the CSD revealed that at least two other Ni(salen) structures  $^{31}$  form similar parallelograms in the solid state with Ni···O $_{\rm phen}$  distances of 2.84 and 3.11 Å, respectively. In all these cases, the interactions detected between Ni(II) and O $_{\rm phen}$  can be concluded to be primarily electrostatic in nature.

Assembly of the noted parallelogram in our structure (i.e., dimerization of [Ni,K]) appears to be further favored by a pair of weak  $C-H\cdots K$  packing interactions that feature long apparent  $H\cdots K$  distances of 2.98 Å. Each of these interactions occurs between one hydrogen (H21B) of the methylene carbon (C21) in the di-imine backbone of [Ni,K] and the

nearby potassium ion. The C-H···K interaction is presumably driven by intrinsically weak packing forces, as the K<sup>+</sup> ion is not drawn toward the C-H bond but rather sits out of the mean plane defined by the crown ether O atoms on the opposite "face" of the  $L_{salmen}$  ligand by 0.74 Å. The observation that  $K^+$ sits out of the plane could be attributable to the presence of the aforementioned bound triflate, which features conventional K-O<sub>triflate</sub> distances of 2.79 and 3.03 Å, as well as what appears to be a weak K···F<sub>triflate</sub> interaction with a distance of 3.26 Å. These interactions appear to assist the triflate ion in occupying the exposed face of the potassium ion, effectively pulling the ion "up" out of the plane of the crown ether and opening space for the nearby methylene C-H moiety to move into the ring of O atoms defining the crown site. As K<sup>+</sup> is by far the largest ion investigated in the [Ni,M] series (see Shannon ionic radii values in Table 1), it can be anticipated that most of these

Table 1. Structural Parameters for the Heterobimetallic [Ni,M] Complexes from XRD Analysis

compound	[Ni] <sup>h</sup>	[Ni,K]	[Ni,Na]	[Ni,Sr] <sup>i</sup>	[Ni,Ca] <sup>i</sup>	[Ni,La]	[Ni,Lu]
$pK_a$ of $[M(H_2O)_m]^{n+a}$		16	14.8	13.2	12.6	9.1	7.9
coordination number (CN) of M		9	7	9	8	10	9
Shannon ionic radius of M (Å) <sup>b</sup>		1.55	1.12	1.31	1.12	1.27	1.03
$N_1 \cdots N_2(\mathring{A})$	2.544(7)	2.524(4)	2.534(11)	2.51(1)	2.50(3)	2.509(17)	2.537(6)
$O_1 \cdots O_2(\mathring{A})$	2.514(5)	2.522(3)	2.457(9)	2.50(1)	2.46(2)	2.495(9)	2.408(4)
$Ni-N_{imine}(A)^{c}$	1.869(4)	1.854(3)	1.850(7)	1.84(1)	1.85(2)	1.845(9)	1.846(5)
$Ni-O_{phen}(\mathring{A})^c$	1.859(4)	1.853(2)	1.842(6)	1.85(1)	1.85(2)	1.862(6)	1.848(3)
$M-O_{phen}(A)^{c}$		2.714(3)	2.393(6)	2.57(2)	2.40(2)	2.522(6)	2.301(3)
$M-O_{3,6}(\mathring{A})^c$		2.790(3)	2.561(8)	2.685(4)	2.60(2)	2.692(5)	2.524(3)
$M-O_{4,5}(\mathring{A})^c$		2.858(3)	2.896(9)	2.688(4)	2.55(2)	2.662(6)	2.434(3)
Ni···M (Å)		3.717(1)	3.426(3)	3.611(3)	3.42(1)	3.561(2)	3.3567(8)
$\omega_{ m salmen}^{d}$		0.112	0.002	0.062	0.045	0.066	0.065
$\omega_{ m crown}^{e}$	0.245	0.107	0.353	0.090	0.371	0.194	0.585
$ au_4^f$	0.072	0.098	0.021	0.057	0.047	0.062	0.072
$\psi_{ ext{Ni}}^{\ m{g}}$	0.002	0.008	0.008	0.009	0.008	0.023	0.014

"From ref 16. "From ref 20. "Defined as the average interatomic distance between the noted metal and the relevant oxygen/nitrogen atoms. "Defined as the root-mean-square deviation (rmsd) of O1, O2, N1, and N2 from the mean plane of their positions. "Defined as the rmsd of the positions of atoms O1, O2, O3, O4, O5, and O6 from the mean plane of their positions. "Geometry index for four-coordinate complexes, with a value of 1.00 indicating perfect tetrahedral geometry and zero indicating completely square-planar geometry. Calculated as described in ref 32. "Absolute value of the distance between Ni and the mean plane of O1, O2, N1, and N2. "From ref 23. 'Average values for [Ni,Sr] and [Ni,Ca] were calculated as the arithmetic mean of the values of the parameters in the structural data. Stated e.s.d.'s on distances for [Ni,Sr] and [Ni,Ca] were taken as the largest of the individual values in the refined data for the particular values corresponding to the given independent molecular species in the refined structural data. See Table S4 for data regarding the independent molecular species.

unique solid-state features are attributable to the relatively large size of this ion in comparison with the size of the crownether-like site in  $L_{\rm salmen}$ . At this point, all the interactions holding the dimeric species together in the solid state appear weak, and thus upon dissolution in solution, one would anticipate the formation of a monomeric species. In the monomeric complex, the polyether chain could reorganize to some extent, rearranging and allowing solvent (MeCN) molecules to bind and fill in gaps in the  $K^+$  coordination sphere in order to achieve a preferred higher coordination number. The triflate could bind in a monodentate or bidentate fashion in solution or even dissociate to yield an overall cationic heterobimetallic species (see pp. \$59–\$60).

Despite these unique solid-state features for [Ni,K], analysis of the structural parameters associated with the Ni(II) ions indicates that the coordination environments of the nickel centers themselves are quite consistent across the [Ni,M] series. The average  $Ni-N_{imine}$  and  $Ni-O_{phen}$  distances are similar (indistinguishable in terms of the  $3\sigma$  criterion) in all of the complexes (see Table 1 and Figure S118), suggesting that the environment of the Ni center does not change significantly upon incorporation of the secondary metals. The coordination geometry of the Ni center remains rather strictly square-planar in all cases, as judged by the  $\tau_4$  geometry indices that remain near zero for all the complexes (see Figure S119).32 The observation of near-zero  $\tau_4$  geometry indices is in accord with quantification of minimal out-of-plane deformation of the N<sub>imine</sub> and O<sub>phen</sub> atoms that define the tetradentate Schiff-base  $[N_2,O_2]$  cavity ( $\omega_{\text{salmen}}$  parameter, see Table 1). The most significant deviation from square planarity for the Ni center is found in the case of [Ni,K], but this deviation can likely be attributed to minor distortions brought about by the dimerization of [Ni,K] in the solid state. The ethylene backbone in the Schiff-base site of L<sub>salmen</sub> appears to have sufficient flexibility to enable one C-H moiety (C21-H21B) found on one methyl group of the backbone to embed into the enclosed volume of the nearby and appropriately shifted

(inversion-related) crown site, allowing for more efficient solid-state packing. As a consequence of this interaction, a torsion is induced in the ethylene bridge and thus translates down the chain to the two imine (donor) groups in the Schiffbase moiety; this effectively out-of-plane distortion clearly drives up the  $\omega_{\rm salmen}$  parameter to 0.112, the highest value of this parameter across the series of complexes [Ni,M]. However, in all cases, there is minimal displacement of the nickel center from the plane defined by ligand donor atoms ( $\Psi_{\rm Ni}$  parameter, see Table 1), showing that the nickel center remains firmly planted in the Schiff-base-site of  ${\bf L_{salmen}}$  in all cases. Considering all of these quantitative metrics, the nickel sites in the complexes appear quite structurally consistent in the solid state.

In contrast with the rather narrow range of metrics for the nickel sites, the structural data from XRD analysis show that the behavior of the secondary metal cations held in the crownether-like  $[O_6]$  site is far more varied across the series. We first noticed this behavior when inspecting the metal-to-oxygen bond distances for the complexes; we found that, as expected, the cations associated with smaller ionic radii display shorter M-O distances in all cases. Regarding the analysis of the average M-O distances, we note here that the large and potentially planar macrocyclic ligand L<sub>salmen</sub> would be C<sub>2</sub>- or  $C_{S}$ -symmetric without the two distal methyl groups on the ethylene bridge of the salen-like site. Thus, we examined the average  $M-O_{phen}$ ,  $M-O_{3,6}$ , and  $M-O_{4,5}$  distances (see Table 1), assuming that the two noted methyl groups would not induce significant structural perturbations across the Ni···M vector in the heterobimetallic species. As expected, the bond distances and angles from the opposing "sides" of the complexes were found to be similar in each case. The average  $M-O_{phen}$ ,  $M-O_{3,6}$ , and  $M-O_{4,5}$  distances all display reliable linear dependences on the Shannon ionic radii of the metal cations (see Figure S116).20 As the oxygen donors are constrained by ethylene linkers within the framework of the macrocyclic ligand L<sub>salmen</sub>, their coordination to M forces the

polyether to flex (or bow) as it wraps around M to (partially) satisfy its preferred coordination number. This behavior can be seen visually in the structures themselves (see Figure 1) but was quantified, as in our prior work, through the  $\omega_{\rm crown}$  parameter (see Table 1). The tendency toward distortion of the macrocycle particularly affects the smaller cations, as in [Ni,Na] ( $\omega_{\rm crown}=0.353$ ) [Ni,Ca] ( $\omega_{\rm crown}=0.371$ ) and most dramatically [Ni,Lu] ( $\omega_{\rm crown}=0.585$ ). Thus, the smaller cations can be concluded to distort the structure of the crownether-like site more dramatically than their larger analogues within each valency. As expected, however, the O1, O2, O3, and O6 atoms in each structure are much closer to being coplanar.

Returning to the M-O distances, we were intrigued upon close inspection of the data to note that the  $M-O_{\text{phen}}$  distances show the greatest dependency on ionic radius among the three classes of symmetry-related distances. The change in average distance (in Å) normalized by ionic radius (in Å; see Figure S116) returns unitless dependencies of  $0.79(\pm 0.04)$  for M- $O_{\text{phen}}$ , 0.77(±0.17) for M-O<sub>4.5</sub>, and only 0.51(±0.04) for M-O<sub>3,6</sub>. Thus, the most significant change was measured for M-O<sub>phen</sub>, and the most modest change was measured for M-O<sub>3,6</sub>. This finding is in accord with the flexible nature of the alkyl ether moieties (containing O4 and O5); these atoms have sufficient structural degrees of freedom to adopt sterically ideal positions on the coordination spheres for the individual secondary cations. On the other hand, the bridging phenoxides (O1 and O2) and aryl-ether oxygen donors (O3 and O6) are held more tightly in place as they are bonded to sp<sup>2</sup>-hybridized carbons within the aromatic portion of the macrocyclic ligand. As a result, the secondary metal cations can draw the alkyl ether donors "inward" while also themselves nestling inward toward the bridging phenoxide donors. As result, the M-O<sub>phen</sub> distances span 0.41 Å in the series, the M-O<sub>4,5</sub> distances span a similar 0.46 Å, and the more rigid M-O<sub>3.6</sub> distances span only 0.27 Å. We hypothesize that the tendency for the metal cations to nestle into the  $[Ni^{II}(\mu_2-O_{phenoxide})M^{n+}]$  diamond cores is driven by a partial anionic character on oxygens O1 and O2, arising from deprotonation of these sites during installation of the nearby Ni(II) center and supporting attractive interactions with the electropositive secondary metal cations.

In accord with these bonding trends for the crown-ether-like site, we have found that the Ni...M distance is linearly dependent on the Shannon ionic radius of the incorporated secondary metal cation. As shown in Figure 2, the smaller metal cations sit closer to the nickel(II) centers in the complexes, whereas the larger metal cations prefer to sit at a greater distance away. This behavior was quantified by the slope (unitless) of the relationship, which has a value of  $0.70(\pm 0.03)$ ; the modest uncertainty on this value corresponds to only 4.3%, in accord with the good correlation displayed in the data ( $R^2 = 0.99$ ). As the disposition of the Ni(II) center in all the complexes appears fixed based on the preceding analysis in this section, the change in the Ni···M interatomic separation can be confidently ascribed to changes wrought by the properties of secondary metal cations; these appear dependent on the ionic radius of M. In line with these observations, the O1···O2 separation also displays a highly correlated but nonlinear dependence on the ionic radius of M (see Figure S120). Thus, the smaller secondary metals draw together O1 and O2 in the complexes, tightening the diamond core motif by nestling more closely into the binding site. In addition,

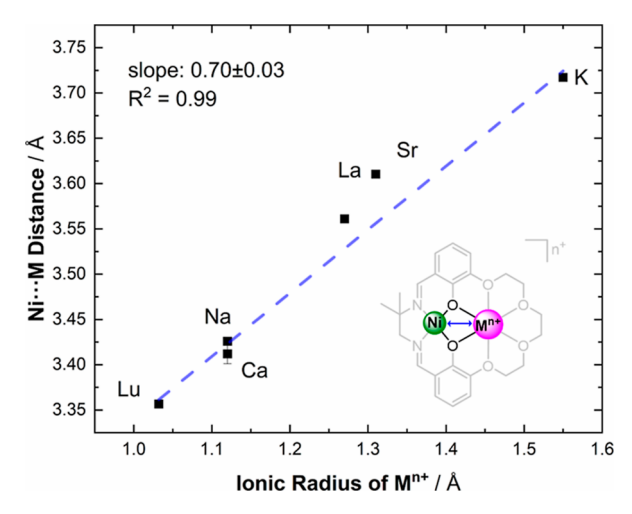


Figure 2. Plot showing the relationship between the  $Ni\cdots M$  distance and the ionic radius of  $M^{n+}$ . The positive trend shows that smaller ions tend to sit closer to the Ni(II) ion.

contrasting with this drawing together of O1 and O2, the N1··· N2 distances remain virtually invariant across the [Ni,M] family of complexes due to the ethylene link between them as well as the covalent nature of the nickel site, which appears to have limited structural degrees of freedom. We also note here that although heterobimetallic complexes based on Reinhoudt-type ligands have been studied by our group and others for a number of years, the dependence of M'···M distance on ionic radius has not before been conclusively established through interrogation of a comprehensive series of complexes (cf. Figure S114 in ref 9).

With the structural data in hand for the isolated forms of the heterobimetallic complexes (featuring the Ni(II) formal oxidation state), we anticipated that one opportunity would lie in quantifying how incorporation of the various secondary metal cations influences the spectroscopic and electrochemical properties of the complexes. As noted by one reviewer of this paper, however, "virtually all measurements in chemistry reflect energy differences between two states, making it difficult to attribute any change in property to interactions in [only] one of the two states." There could be myriad structural (e.g., bond length changes) or electronic (e.g., change in dipole moment) changes upon excitation with light, as in electronic absorption spectroscopy, or upon reduction, as in the electrochemical work. As an intermediate strategy to approach the challenge posed in understanding how secondary metals tune the properties of heterobimetallic complexes, we sought to catalog the spectroscopic and electrochemical properties that can be measured with our isolated complexes in light of electron paramagnetic resonance (EPR) data (reported here) that support the viability of generation of 1e<sup>-</sup> reduced species from the isolated Ni(II) forms of the complexes (vide infra). Our interpretations regarding the origins of the tunability among the complexes are presented here as tentative, however, because the primary lens through which these effects have been interpreted is the structural data obtained for the isolated Ni(II) complexes only.

Electronic Absorption Spectroscopy. Cation-induced shifts in both CT and d-d transitions are typically observable in square-planar nickel(II) complexes of Schiff-based-type ligands.<sup>33</sup> Regarding identification of these transitions for [Ni], the d-d transition could be assigned as corresponding to the

feature near 550 nm due to its position as well as modest molar absorptivity value ( $\varepsilon=100~{\rm M}^{-1}~{\rm cm}^{-1}$ ). The anticipated CT transition was found at 418 nm and was assigned on the basis of its larger molar absorptivity value ( $\varepsilon=4500~{\rm M}^{-1}~{\rm cm}^{-1}$ ). Similar features were measured for all the heterobimetallic species, albeit shifted in each case to higher energies, similar to observations made in prior work (see Figures S40–S66).  $^{8-10,34}$ 

Upon cation incorporation, both the d-d and CT transitions undergo blue shifts relative to the precursor complex [Ni]. As shown in Figure 4, the CT transitions

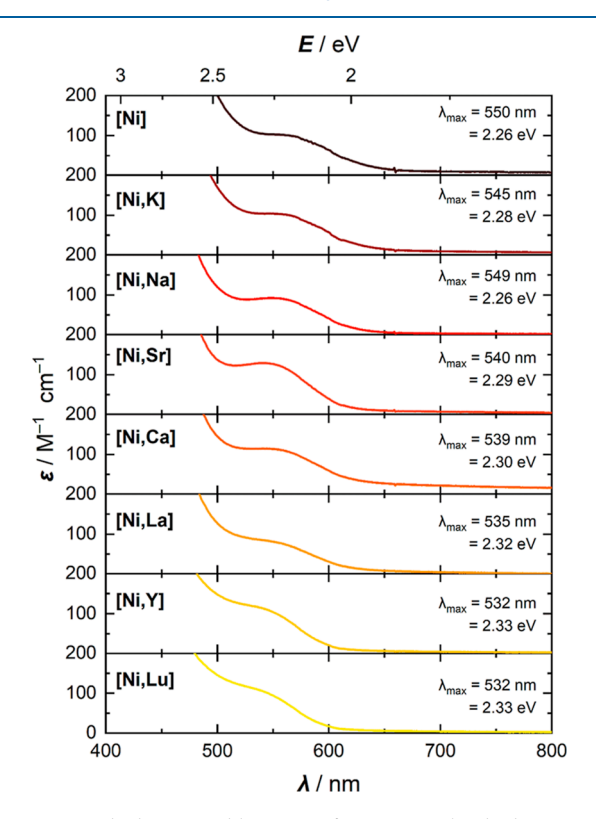


Figure 3. Stacked UV-visible spectra focusing on the d-d transitions noted for [Ni] as well as each compound in the [Ni,M] family.

undergo a shift from 418 nm for [Ni] to 370 nm for [Ni,La], whereas the d-d transitions shift more modestly from 550 to 535 nm for the same range of complexes as can be seen in Figure 3. Plotting the energies of both the CT and d-dtransitions as functions of the Lewis acidity values corresponding to each secondary metal cation (p $K_a$  values of the respective aqua ions) reveals reasonable linear dependencies in each case, as shown in Figure 5, of  $-36 \pm 5$  meV/pK<sub>a</sub> for the CT transition and  $-7.7 \pm 1.3 \text{ meV/p}K_a$  for the d-d transition. On the one hand, the shift in the CT transition is similar to those we have measured for other families of complexes supported by  $L_{salmen}$  containing the vanadyl ion  $^{10}$  ([VO]<sup>2+</sup>;  $-30 \pm 5 \text{ meV/p}(K_a)$  and palladium(II)<sup>9</sup> ( $-45 \pm 3 \text{ meV/p}(K_a)$ ). On the other hand, the d-d transition energy appears markedly less sensitive to the effects of the secondary metal. This could indicate more similar cation effects on the individual donor and acceptor orbitals involved in the d-dtransition (versus those involved in the CT transition), but at this stage, we will not speculate further.

For comparison, however, we mention that the d-d transitions in the noted vanadyl complexes<sup>10</sup> underwent a cation-driven shift of  $-50 \pm 10$  meV/p $K_a$ , a value over  $7 \times$ 

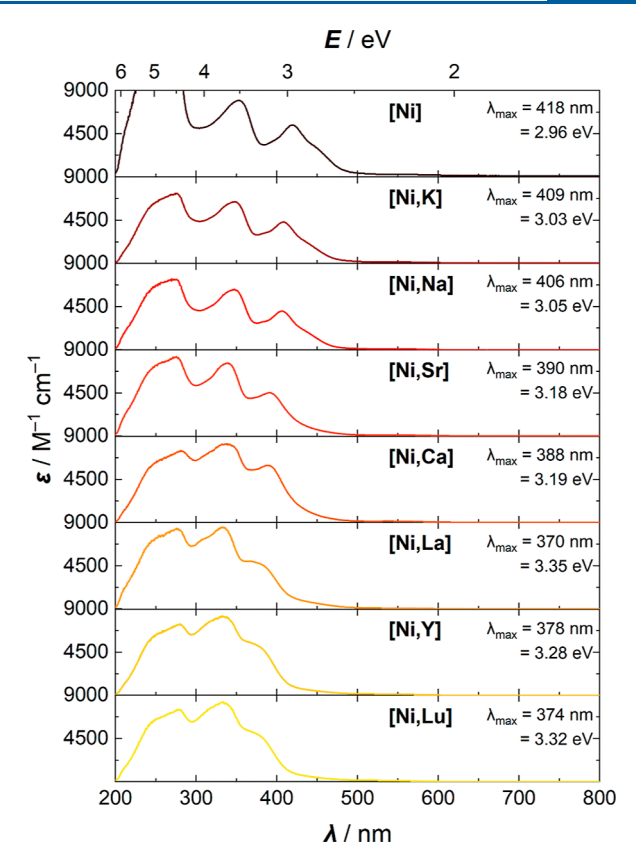


Figure 4. Stacked UV–visible spectra focusing on the CT transitions noted for [Ni] as well as each compound in the [Ni,M] family.  $\lambda_{\text{max}}$  values for the species incorporating trivalent cations were obtained through peak deconvolution (see the Supporting Information, p. S33–S37).

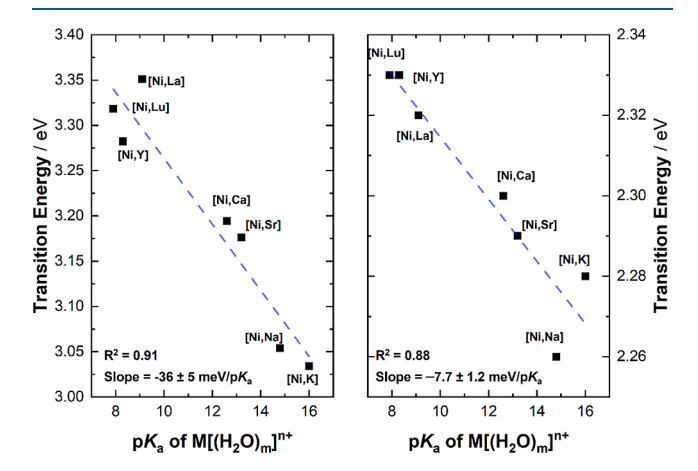


Figure 5. Plots showing the dependence of the studied transitions (left, CT; right, d-d) of [Ni] and the [Ni,M] family on the Lewis acidity of the associated secondary metal.

greater than that found in the Ni(II) complexes here. This difference, however, can be readily ascribed to greater structural flexibility in the vanadyl complexes. The nickel complexes are structurally invariant about the Ni(II) centers themselves, as the Schiff-base binding sites remain rigorously square planar (as quantified by  $\tau_4$ ), and the metal centers remain firmly bound in the plane defined by N1, N2, O1, and O2 (as quantified by  $\psi_{\rm Ni}$ ). The average Ni–O<sub>phen</sub> and Ni–N<sub>imine</sub> distances also shift very little across the full series of Lewis acid adducts. Conversely, the vanadyl moiety in the

Table 2. Electrochemical Characteristics of [Ni] and [Ni,M]

compound	$pK_a$ of $[M(H_2O)_n]^{n+a}$	$E_{1/2}$ (V)	$\Delta E_{1/2}$ vs [Ni] (mV) <sup>b</sup>	$\Delta E_{\rm p}  \left({\rm mV}\right)^{b}$	$k^0 (\text{cm/s} \times 10^3)^c$	$\%~V_{ m f}$
[Ni]		-2.14	0	84	$6.4 \pm 0.3$	45.8
[Ni,K]	16	-1.95	190	82	$7.9 \pm 0.3$	36.5
[Ni,Na]	14.7	-1.95	190	77	$7.4 \pm 0.6$	39.6
[Ni,Sr]	13.2	-1.68	460	81	$8.1 \pm 0.3$	37.4
[Ni,Ca]	12.7	-1.68	460	78	$8.2 \pm 0.3$	36.5
[Ni,La]	9.1	-1.42	720	88	$6.2 \pm 0.3$	30.7
[Ni,Y]	8.3	-1.45	690	103	$3.7 \pm 0.2$	
[Ni,Lu]	7.9	-1.43	710	110	$3.5 \pm 0.2$	24.5

<sup>a</sup>From ref 16. <sup>b</sup>Measured at 100 mV/s. <sup>c</sup>Average value reported is the arithmetic mean of the values determined at eight different scan rates (50, 100, 150, 200, 250, 300, 500, and 1000 mV/s). Uncertainty (reported as  $\pm 1\sigma$ ) was calculated from the replicate data.

[VO,M] complexes undergoes significant structural changes upon incorporation of secondary metal cations. For example, the average V–O<sub>phen</sub> distance elongates from 1.924(1) Å for [VO] to 1.94(1) Å for [VO,Ca]. Moreover, the V–O<sub>oxo</sub> bond shortens upon incorporation of Na<sup>+</sup> or Ca<sup>2+</sup>, shifting from 1.605(1) Å in [VO] to 1.595(7) in [VO,Na] and 1.59(1) Å in [VO,Ca]. These changes in the first coordination sphere could contribute to the more substantial changes in the d–d transition energies; the contraction of the V–O<sub>oxo</sub> distance should induce the oxo ligand to serve as a stronger  $\sigma$ - and  $\pi$ -donor, widening the span of d-orbital energies and driving the noted blue shift. Of course, the electronic configurations involved in the d-d transitions for the Ni<sup>2+</sup> and [VO]<sup>2+</sup> cases are notably distinct in each case;  $3d_{x^2-y^2}$  or  $3d_{xy}$  are the likely acceptors for the Ni(II) case and the likely donors for the [VO]<sup>2+</sup> case. <sup>33,35</sup>

Electrochemical Studies. Beyond the aforementioned challenge of attributing changes in electrochemical properties to specific cation-promoted effects when both the oxidized and reduced forms of the complexes are not available for direct interrogation, follow-up chemical reactivity associated with redox cycling also often causes complications in data analysis. For example, in our prior work with nickel complexes, the Ni(II)/Ni(I) reduction of interest was chemically irreversible, precluding studies of the reduced forms.<sup>5,36</sup> Similarly, when studying the V(IV)/V(V) oxidations for the [VO,M] series, cation-dependent irreversibility was encountered, suggesting oxidation-induced speciation that might involve loss of the secondary cations upon oxidation.8 The use of the L<sub>salmen</sub> ligand system here has assisted in avoidance of such complications, as reduction processes for nickel(II) complexes based on salen-type ligands have been found in prior work to display chemical reversibility in cyclic voltammetry, 13,37 and corresponding reductions have been found to be reversible here as well. All past studies from our group aimed at interrogation of the properties of adducts with trivalent cations have been impacted by irreversible electrochemical behaviors, 5,8-10,34,38 motivating the present study to interrogate changes wrought by incorporating trivalent cations.

Starting with the monometallic precursor complex [Ni], cyclic voltammetry (CV; see Table 2) revealed a quasi-reversible couple centered at  $E_{1/2} = -2.14$  V vs the ferrocenium/ferrocene couple (hereafter denoted as  $\mathrm{Fc}^{+/0}$ ). Both the cathodic and anodic waves remain observable across the multiple scan rates utilized here (see Figure S70), in accord with formation and persistence in solution of a  $\mathrm{Ie}^-$  reduced form of the complex; the electrogenerated complex, which would display a formal nickel oxidation state of +I, persists on the time scale of the CV experiment. Appealingly, scan-rate-

dependent studies over the range of 50–1000 mV/s confirmed freely diffusional behavior at the electrode for both the oxidized and reduced forms of the compound; this is consistent with the good solubility of the complex in MeCN-based solutions. Additionally, we note here that the peak-to-peak separation of the cathodic and anodic waves (hereafter denoted  $\Delta E_{\rm p}$ ) was found to be 84 mV when measured at 100 mV/s, consistent with relatively fast ET behavior in the organic electrolyte used here. <sup>39</sup>

We interrogated the heterobimetallic complexes similarly to check for any relationship between the identity of the incorporated secondary metal cation and the thermodynamic reduction potential. Each redox couple measured for the complexes [Ni,M] (see Figure 6) exhibited reversible reductions shifted to thermodynamic potentials more positive than that measured for [Ni]. This behavior qualitatively matches prior fundings from Yang and co-workers on monoand divalent cation adducts, 13 as well as our work on related complexes based on a more conjugated ligand denoted as  $L_{\text{salben}}$ . The thermodynamic  $E_{1/2}$  values shift based on the

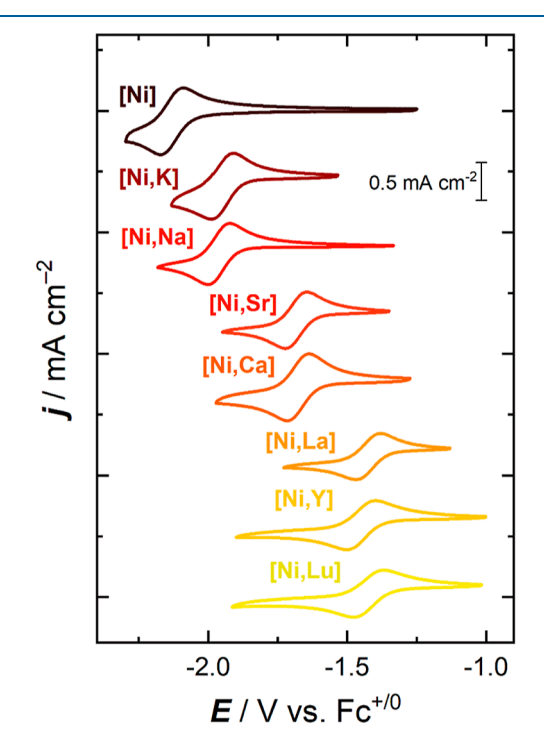


**Figure 6.** Stack of the cyclic voltammograms for [Ni] and the [Ni,M] family. All scans were taken at a scan rate of 100 mV/s at a concentration of 2 mM in acetonitrile (0.1 M TBAPF<sub>6</sub>).

charge (rather than Lewis acidity or another descriptor) of the incorporated secondary metal cation. The monovalent and divalent cations display identical  $E_{1/2}$  values of -1.95 and -1.68 V, respectively, and the trivalent cations display very similar  $E_{1/2}$  values spanning the narrow range from -1.42 to -1.45 V (see Figure 7). In all cases, the oxidized and reduced

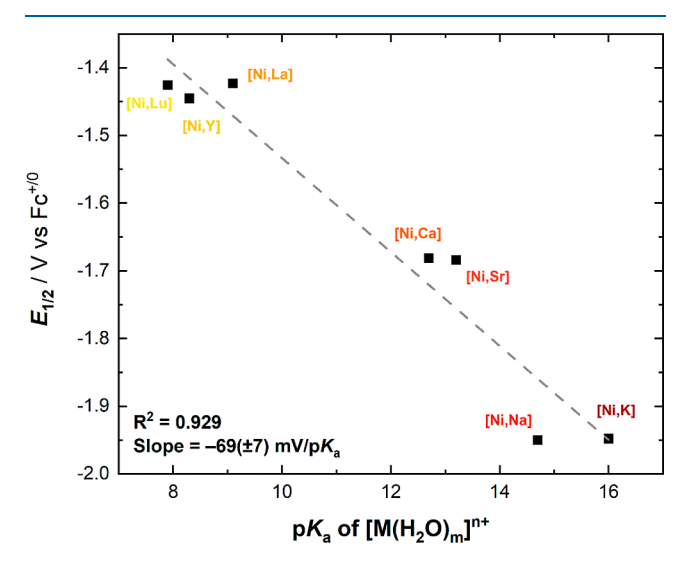


**Figure 7.** Plot of the  $E_{1/2}$  of the [Ni,M] family vs the p $K_a$  value of the relevant M aqua complexes. Notably, charge appears to be the dominant factor in determining  $E_{1/2}$ .

forms of the complexes were shown through scan-rate-dependent studies to be freely diffusional at the working electrode surface, confirming that there is no apparent influence on this data of secondary surface adsorption or chemical reactivity phenomena (see pp. S41–S48).

Interpreting the precise origin of the tunable reduction potential for the [Ni,M] complexes is not possible without structural (or spectroscopic) data for the reduced analogues of the isolated Ni(II) complexes. Cation-induced electric fields, cation-driven structural deformations, size-dependent phenomena, and solvation differences could contribute to the free energy differences between the oxidized and reduced species in each case. Some systems that undergo metal-centered redox have shown linear correlations between reduction potentials and secondary cation Lewis acidities (as judged by the  $pK_a$ values of the corresponding aqua complexes) rather than charge-dependent behaviors. 8-10,38,40 Plotting the reduction potential values as a function of the Lewis acidity ( $pK_a$  values) of the corresponding secondary metal cations in the data reported here, however, reveal a clear "stair-step" appearance in the data (see Figure 7). Nonetheless, the slope of the apparent dependence on Lewis acidity in the data is  $-69 \pm 7 \text{ mV/p} K_a$ , very similar to values to from our prior work on nickel $^{5}$  (-70  $\pm$  12 mV/p $K_a$ ) and uranyl<sup>8</sup> (-61  $\pm$  9 mV/p $K_a$ ) complexes. The magnitude of the slope is also greater than those measured for ligand-centered reduction processes in palladium<sup>9</sup> and complexes of  $-41 \pm 3$  and  $-48 \pm 3$  mV/p $K_a$ respectively. We emphasize that 1e reduction potentials are determined by the properties of both the oxidized and reduced forms<sup>41</sup> of the complexes being studied, and as structures of the Ni(I) forms of the complexes studied here are not available at this time, we hesitate to comment further on the tunable thermodynamics. However, during peer review, one reviewer noticed that the slope of the linear correlation in Figure 7 is

close to unity (1.17 to be precise) when the  $pK_a$  scale is converted to the same units as  $E_{1/2}$  according to  $2.303 \cdot RT \cdot log(K_a) = 59.1$  mV; 69/59 = 1.17. This relationship could be indicative of charge density effects being operative in this system, wherein the cationic charge of the secondary cations exerts an electrostatic influence over, of primary importance, the phenoxide moieties that bridge to the nickel center. <sup>10,38</sup> In such a case, the phenoxide O atoms could be subject to an influence from the secondary metal cations that is not unlike the influence cast over the coordinated water molecules in the metal—aqua complexes for which the  $pK_a$  values were tabulated. <sup>16</sup>

**EPR Studies.** In light of the importance of the reduced forms of the [Ni,M] complexes to this study, we pursued X-band EPR characterizations that could directly establish the accessibility of reduced forms of heterobimetallic species. Each of the isolated nickel(II) complexes is diamagnetic, featuring a  $3d^8$  configuration and an S=0 ground state. However, the 1e<sup>-</sup> reduced forms of the complexes were anticipated to be paramagnetic, with S=1/2 ground states, and featuring  $3d^9$  configurations in the case of metal-centered reduction to generate the Ni(I) formal oxidation state. (All of the secondary metal cations used here are intrinsically diamagnetic.)

Treatment of [Ni,Lu], [Ni,Ca], and [Ni,K] with 1 equiv of  $Cp*_2Co$   $(E_{1/2} = -1.91 \text{ V in MeCN}^{42})$  resulted in the appearance of new signals in all cases that are consistent with generation of paramagnetic species. 43 Appealingly, the oxidized form of the chemical reductant used here is the diamagnetic species  $[Cp*_2Co]^+$ ; this species does not contribute any signals to the EPR data, simplifying interpretation of the spectra. In the cases of the spectra obtained upon reduction of [Ni,Lu] and [Ni,Ca], the distinctive isotropic signal near g = 1.8associated with the chemical reductant Cp\*2Co (see Figure S93) was completely absent, consistent with complete ET to the nickel complexes in these two cases. This is consistent with the electrochemical data, in that the reduction potentials for these two complexes are well positive of that for Cp\*2Co+/  $\text{Cp*}_{2}\text{Co }(\Delta E_{1/2} = 0.47 \text{ and } 0.22 \text{ V, respectively}). For [Ni,Lu],$ a relatively narrow set of features was observed between g = 2and 2.1. For [Ni,Ca], a similar result was obtained, although there appear to be two overlapping sets of spectral features between g = 2 and 2.1. In the case of the spectrum obtained upon treatment of [Ni,K] with 1 equiv of Cp\*2Co, a more complex set of features were observed that include a contribution of unreacted Cp\*2Co. However, there is a clear new set of signals in the data between g = 2 and 2.3, consistent with ET to generate nickel(I) species. Notably, this is consistent with the measured reduction potential for [Ni,K] at -1.95 V; this potential, although negative of the formal potential for Cp\*2Co+/Cp\*2Co, is close enough to support partial reduction of nickel complex upon addition of 1 equiv of Cp\*2Co (theoretically near 50% based on the electrochemical data).

The experimental EPR spectra of the in situ-reduced species were successfully modeled (see Figure 8) with the EasySpin software package. The spectral profile of the data corresponding to reduction of [Ni,Lu] was well reproduced by a single S = 1/2 system displaying axial symmetry. A small, narrow feature apparent at g = 1.997 could be ascribed to formation of a small amount of an S = 1/2 organic radical species, either arising from decomposition or adventitious contamination; 98% of the spectral intensity in the model is attributable to the axial species, while 2% is attributable to the

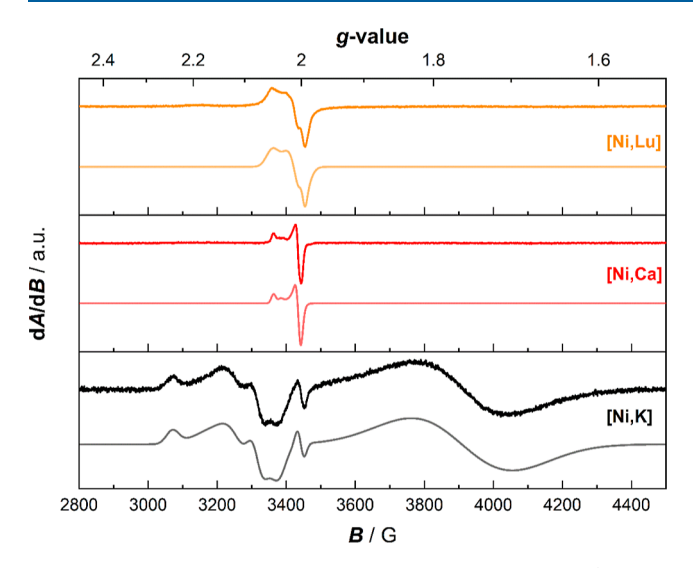


Figure 8. X-band continuous-wave EPR spectra of [Ni,Lu] (orange; simulated spectrum in light orange), [Ni,Ca] (red; simulated spectrum in light red), and [Ni,K] (black; simulated spectrum in gray). The experimental spectra were collected in frozen acetonitrile at ca. 4 K.

minor organic radical. The data for [Ni,Ca] could be modeled similarly, and the spectrum was well reproduced with a mixture of two components; in this case, both components are S=1/2 systems displaying axial symmetry. Component I (77%) has main features at the *g*-values of 2.048 and 2.003, whereas component II (23%) has one unique feature at g=2.035 and a second feature that overlaps with the spectral feature of component I at g=2.003. We anticipate that the observation of multiple species could be attributable to triflate ligand reorganization or dissociation upon reduction; the reduced form of [Ni,Ca] would be anionic with all triflate ligands bound.

The final model for the spectrum obtained upon reduction of [Ni,K] included four individual components, including an axial S = 1/2 system with features at g = 2.242 and 2.102 (component I; 7%) and a rhombic S = 1/2 system with features at 2.171, 2.078, and 2.040 (component II; 10%). We anticipate that these two different signals arise from reduced species that differ only in binding of the triflate counteranion to the  $K^+$  center. The broad signal near g = 1.762 could be modeled and assigned as arising from unreacted Cp\*2Co (corresponding to 83% of the spectral intensity), and a very sharp signal located at g = 2.001 could be modeled and assigned as an S = 1/2 organic radical species (<1%). As in the case of the work with [Ni,Lu], we anticipate that this organic radical component arose due to decomposition or adventitious contamination. The observation of unreacted Cp\*2Co in the spectrum collected for [Ni,K] is in accord with the rather negative reduction potential of the nickel complex ( $E_{1/2}$  = -1.95 V).

The observation of axial spectral profiles for the species generated upon reduction of [Ni,Lu] and [Ni,Ca], and axial/rhombic signals for [Ni,K] could be consistent with metal-centered reduction to form nickel(I) species. However, the *g*-dispersion is significantly greater for the species generated by reduction of [Ni,K] ( $\Delta g = 0.140$  and 0.130) than in the cases of [Ni,Ca] ( $\Delta g = 0.045$  and 0.032) and [Ni,Lu] ( $\Delta g = 0.050$ ). Prior examples of spectra for nickel(I) complexes display significant *g*-dispersion, with features in the spectra spanning

several hundred Gauss. An One reviewer of this paper also provided the helpful suggestion of comparing the g-dispersion in the spectra collected here to values obtained in spectra for four-coordinate d9 Cu(II) complexes; spectra for such complexes are generally axial with g-values spanning from  $\sim\!2.05$  to  $\sim\!2.25$ , corresponding to  $\Delta g=0.20$ . Considering all this, we anticipate that the spectra collected here are consistent with some ligand radical character in the formally nickel(I) species, particularly for the derivatives containing Ca^{2+} and Lu^{3+}. This conclusion is based on the noted g-dispersion trends as well as the known propensity of salen- and salophen-type frameworks to display ligand involvement in reduction processes, leading in some cases to significant unpaired spin density on the imine moieties and reactivity at those positions.

**Determination of Heterogeneous ET Rates.** Returning to the electrochemical studies, the peak-to-peak separation of the cathodic and anodic waves for  $[Ni,M]/[Ni,M]^-$  redox are greater for the three adducts of trivalent cations  $(La^{3+}, Y^{3+}, and Lu^{3+})$  than for any of the other complexes studied. The waves for the trivalent cations appear broader than those measured for adducts of weaker Lewis acids (see Figure S85). As demonstrated by Nicholson<sup>46</sup> and elaborated upon by Savéant and Costentin,<sup>41</sup> an increase in peak-to-peak separation for couples measured under identical conditions and displaying similar diffusion coefficients can be attributed to diminished values of the rate of heterogeneous ET (denoted as  $k^0$ ). Diminished values of  $k^0$  in turn can be attributed to diminished exchange current densities and processes involving significant reorganization upon ET.<sup>39</sup>

To quantify this phenomenon, the heterogeneous ET rates  $(k^0)$  associated with each couple were determined using the traditional method from Nicholson that employs a standard working curve to relate measured  $\Delta E_{\rm p}$  values to  $k^0$ . To confirm the accuracy/precision of the measurements made here, the values of  $k^0$  were measured at eight different scan rates and tabulated as an average value (see Table 2). The values of  $k^0$ were found, as expected, to show only minor variation across scan rates (see Figure S86). With this method, we found the  $k^0$ value for [Ni] to be relatively fast at  $6.4 \pm 0.3$  cm s<sup>-1</sup>, while the value for [Ni,Lu] was cut almost in half to  $3.5 \pm 0.2$  cm s<sup>-1</sup> (see Table 2). For the heterobimetallic complexes, a monotonic relationship can be observed between the  $k^0$  values and the p $K_a$  values corresponding to the agua complexes of the incorporated secondary metal cations (see Figure 9). The  $k^0$ values for the derivatives incorporating mono- and divalent secondary metals appear in the data as a "plateau" with essentially "fast" ET behavior, in that the  $k^0$  values for these complexes are indistinguishable within the precision of the measurements. However, incorporation of the trivalent cations slows the rate of ET for [Ni,La]  $(6.2 \pm 0.3 \text{ cm s}^{-1})$  and even more significantly for [Ni,Y] and [Ni,Lu] (3.7  $\pm$  0.2 and 3.5  $\pm$  $0.2 \text{ cm s}^{-1}$ , respectively).

The foregoing observations suggest that one or more factors associated with incorporation of the trivalent cations drive the modestly diminished ET rates to the heterobimetallic complexes in the [Ni,M] series. In order to examine the possible origins of the diminished  $k^0$  values, we turned to the Marcus model for ET.  $^{47-50}$  In this model, following Bard's treatment,  $^{51}$  the standard heterogeneous ET rate will have the general form shown in eq 1

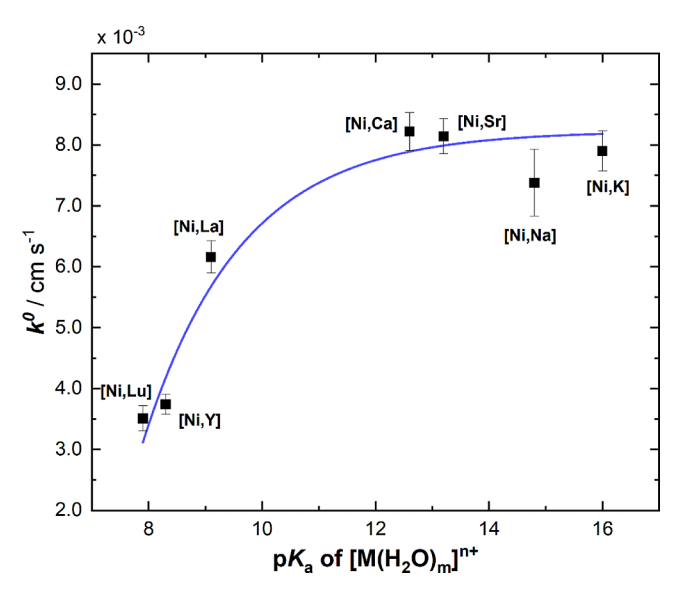


**Figure 9.** Plot of the heterogeneous ET rate  $k^0$  for the [Ni,M] complexes vs the  $pK_a$  of the corresponding  $\mathbf{M}^{n+}$  aqua complex. Values and uncertainties for the  $k^0$  values were determined as described in Table 2. The blue line is intended only to guide the eye and is an exponential decay function.

$$k^{0} = \nu_{N} \kappa_{E} \exp\left(-\frac{\Delta G^{\ddagger}}{RT}\right) \tag{1}$$

This expression relates the standard heterogeneous ET rate constant  $(k^0)$  to a number of quantities, including a nuclear frequency factor  $(\nu_{\rm N})$ , an electronic transmission coefficient  $(\kappa_{\rm E})$ , and the activation free energy barrier for ET from the electrode to the molecular species undergoing reduction/oxidation. The activation free energy,  $\Delta G^{\ddagger}$ , can be broken into two terms. The first is the inner-sphere reorganization of the reactants  $(\lambda_{\rm inner})$ , corresponding to the molecular structural changes upon reaction. The other refers to the outer-sphere solvent reorganization  $(\lambda_{\rm outer})$ , as shown in eq 2

$$k^{0} \propto \exp\left(-\frac{\Delta G^{\ddagger}}{RT}\right)$$

$$= \exp\left(-\frac{1}{4RT}(\lambda_{\text{inner}} + \lambda_{\text{outer}})\right)$$

$$\simeq \exp\left(-\frac{\lambda_{\text{outer}}}{4RT}\right)$$
(2)

Although we note here that the main contribution to  $\Delta G^{\ddagger}$  is conventionally expected to be solvent reorganization (hence the simplification made in removing  $\lambda_{\text{inner}}$  from the latter portion of eq 2), one could estimate  $\lambda_{\text{inner}}$  by examining bond length changes. <sup>52</sup> Here, structural data for the reduced complexes are not available, precluding this estimation. (The electrode itself undergoes virtually zero reorganization upon ET, thus making a negligible contribution to  $\Delta G^{\ddagger,53,54}$ ) The nuclear frequency factor  $(\nu_N)$  is associated with the formation of the encounter complex at the electrode surface, including solvent dynamics in polar media, while the electronic transmission coefficient  $(\kappa_E)$  would be taken as unity under the assumption that the ET reaction proceeds adiabatically, that is, without a limitation due to suboptimal electronic coupling  $(H_{\text{electronic}})$ . <sup>47,48,50</sup> Modulation of one or more of

these quantities across the series of [Ni,M] complexes could lead to the modulated  $k^0$  values that we have measured.

**Topological Map Generation and Analysis of Steric Congestion.** As the identity of the secondary metal cations modulates the  $k^0$  values modestly, we anticipated that the structural data from XRD (see Figure 1 and pp. S57–S87 for details) might offer an explanation for the observed trend. We postulated that the region near the nickel center in each complex would be the most important for investigation; the EPR studies provided evidence for  $\mathrm{Ni}(\mathrm{II})/\mathrm{Ni}(\mathrm{I})$  redox, perhaps with significant ligand radical character in the reduced species featuring divalent and trivalent cations. Consequently, we anticipated that the ET behavior of the complexes would be most affected by the microenvironments (first and secondary coordination spheres) near the nickel centers in each of the heterobimetallic species.

The square-planar first coordination sphere about nickel is highly conserved across the complexes. Only the structure of [Ni,Lu] revealed another possible covalent interaction of the nickel center with a donor ligand, in that one triflate (associated with S2) could be serving in the solid state as a bridging ligand between the nickel and lutetium centers. There is a potential weak interaction with a Ni···O<sub>triflate</sub> distance of 2.908(6) Å (Ni···O23), reminiscent of a similar Ni···O<sub>triflate</sub> motif of ca. 2.786(7) Å that we previously observed with a [Ni,Y] complex-based  $L_{salben}$  (a macrocyclic salophen species).<sup>5</sup> For context, a search of the Cambridge Structural Database<sup>26</sup> to examine intermolecular contacts between Ni in Schiff-base ligand environments and O atoms at distances of 1.75-4.00 Å revealed 292 hits with Ni···O distances spread across the entire range with, of course, more entries on the long distance end of the range. A more specific search for nickel salen or salophen complexes interacting with axially bound fifth ligands to nickel revealed only four examples with Ni···O distances spanning a narrower range of distances from 1.79 to 2.41 Å. 27-30 Thus, the distance of 2.908(6) Å in the complex prepared here appears rather long. We anticipate that this Ni···O23 contact in the solid-state structure of [Ni,Lu] represents a marginal electrostatic interaction rather than a strong dative bond. This conclusion is supported by the formal 18e count of the Ni(II) metal center with only four covalently bound donor ligands.

Instead of a bonding preference at Ni(II), the coordination properties of the heteroditopic macrocyclic ligand  $L_{salmen}$ appear to drive an increase in steric congestion about the nickel site upon binding of trivalent cations in the crown-etherlike site. In particular, there is a structural consequence of the dependence of the Ni...M separation on ionic radius (Figure 2.) This consequence also results from the high coordination numbers associated with the trivalent cations (CN = 9 for [Ni,Lu] and 10 for [Ni,La]), in that two of the bound triflate counteranions in both the structures of [Ni,Lu] and [Ni,La] appear to be forced into cantilever-like positions above and below the plane defined by the Schiff-base site containing nickel (see Figure S140). In the case of [Ni,Lu], O23 and F13 are located, respectively, 2.908(6) and 3.054(7) Å away from the nickel center on opposite sides of the macrocyclic complex. In the case of [Ni,La], atoms F32 and O23' are located, respectively, 3.30(1) and 3.70(3) Å from nickel. The two nextshortest contacts for the other complexes between the Ni centers and triflate-associated atoms are 3.80(1) Å for O11B (3.855(8) Å for O11A) in [Ni,Ca] (see Figure S139) and 3.951(4) Å for F13 in [Ni,K] (see Figure S138). K<sup>+</sup> features a

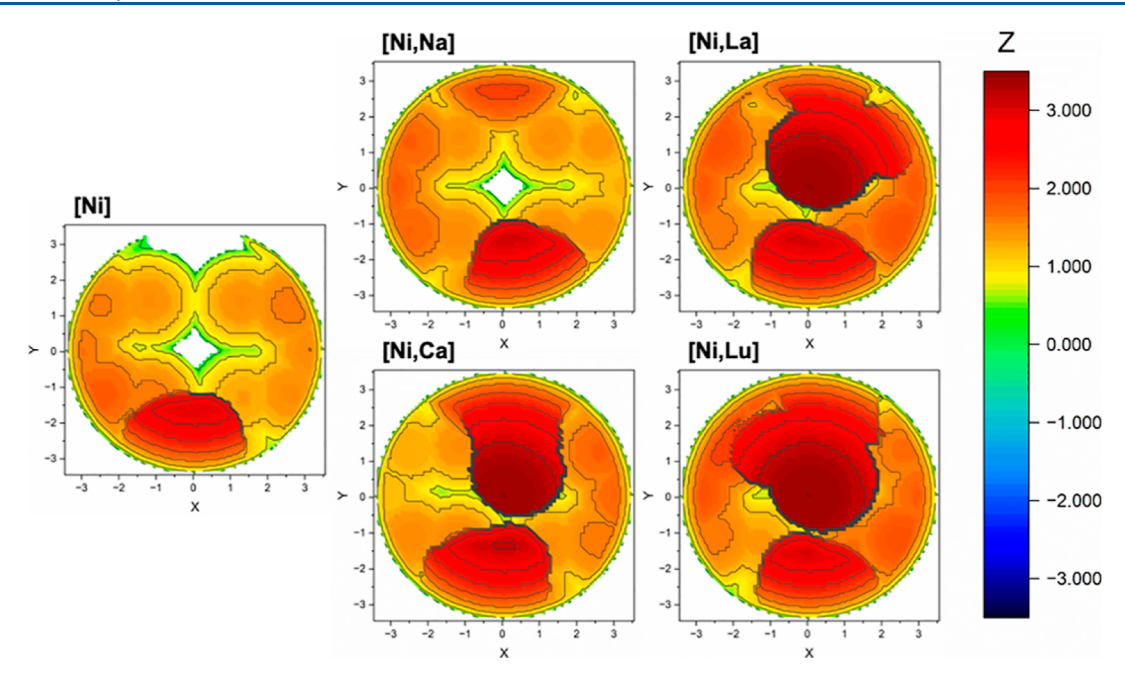


Figure 10. Set of topographic buried volume plots of monomeric [Ni], [Ni,Na], [Ni,Sr], [Ni,La], and [Ni,Lu]. The topographical analysis was carried out with unscaled Bondi radii (1× values) and explicit hydrogen atoms from XRD included. (See pp. S103–S106 for details, including Figure S143 and Table S7.).

larger ionic radius than Lu<sup>3+</sup> and La<sup>3+</sup>, and [Ni,K] resembles these complexes in that it also features a high CN of 9 (see p. \$59-\$60 for discussion); this highlights the importance of higher coordination numbers in amplifying steric crowding in these systems. As the crown-ether-like site is located adjacent to the Schiff-base site, decreased Ni···M separation enables the triflate counteranions to enter the secondary coordination sphere near the Ni(II) center; this effect is enhanced by the macrocyclic nature of the  $L_{salmen}$ , as the crown ether is moved asymmetrically in an out-of-plane distortion upon binding of La(OTf)<sub>3</sub> and Lu(OTf)<sub>3</sub> to accommodate the bound triflate counteranions ( $\omega_{crown}$  = 0.194 and 0.585). In the structures of both adducts, the crown is "pushed" by the two triflates binding to the trivalent cation on the same side toward the opposite face of the crown on which only a single triflate is bound. However, this "push" of the polyether chain toward the opposite face in turn encourages the lone triflate on that opposite face to push into the secondary coordination sphere of the nickel center. Consequently, the trivalent cations appear to uniquely engender enhanced steric crowding in the secondary coordination sphere of nickel.

Quantification of the cation-dependent change in the environment about the nickel centers was carried out using Cavallo's SambVca webtool. 55,56 In particular, the webtool was used to generate topographical steric maps and calculate the percent buried volume (%  $V_b$ ) about the nickel metal centers. As all but one of the complexes were characterized by singlecrystal XRD, this data could be used to understand the filling of space about the nickel centers with steric bulk from atoms associated with triflates and the macrocyclic ligand framework. Additional confirmation of triflate binding in solution remains a topic for future work, and we note here that the conclusions drawn regarding the nickel microenvironments could be impacted somewhat by solvent binding or other changes in the coordination spheres of both nickel and secondary cations. Nonetheless, inspection of the topographical maps generated from the coordinates determined by XRD (see Figure 10 and

pp. S88–S90) shows that the nickel centers (placed at the 0,0 position in the x,y plane) are more open for [Ni] and the derivatives incorporating mono- and divalent cations. In the axial direction, space is noticeably filled by atoms associated with bound triflates as well as a single methyl group from the 1,1-dimethyl-1,2-ethylenediamine-derived ligand backbone in each case that extends into the "upper" hemisphere (in the + z direction set in SambVca as shown in Figures 10 and S129). Steric crowding is also present in the "lower" hemisphere (see Figure S130) but contains only a negligible contribution from the other backbone methyl group, as it is oriented outward away from nickel metal center in each case.

Influences of individual chemical moieties in the heterobimetallic complexes on the percentage of free volume (%  $V_f$ ) were tabulated and are given in Table S5. % V<sub>f</sub> is directly related to %  $V_{\rm b}$  according to the expression %  $V_{\rm f}$  = 1 - %  $V_{\rm b}$ . The "upper" methyl groups on the di-imine bridge of the macrocyclic ligand contribute only 2-3% of the buried volume for all of the nickel species, consistent with the apparent rigidity of the immediate environment about the Ni center. The impact of the triflate counteranions varies markedly across the series, with the greatest influence arising in [Ni,Lu] and [Ni,La], as expected. Between these two cations, smaller Lu<sup>3+</sup> induces greater out-of-plane distortion induced in the crown than La<sup>3+</sup> ( $\omega_{\text{crown}}$  = 0.585 vs 0.194 Å, respectively), forcing two triflates toward the nickel center. In line with this observation, bowing of the macrocyclic ligand is apparent to the eye in the XRD structure of [Ni,Lu] (see Figure 1). Thus, [Ni,La] and [Ni,Lu] were verified to feature the most triflate- and ligandderived steric congestion about the nickel centers, but removal of the methyl groups from the di-imine bridge would not make a substantial difference in steric congestion in any case.

Considering all this, the percent buried volume (%  $V_{\rm b}$ ) and the related percent free volume (%  $V_{\rm f}$ ) as determined with SambVca afforded a descriptor for the influence of the salts of the trivalent cations on the nickel microenvironment. We thus plotted  $k^0$  as a function of %  $V_{\rm f}$  as shown in Figure 11. The

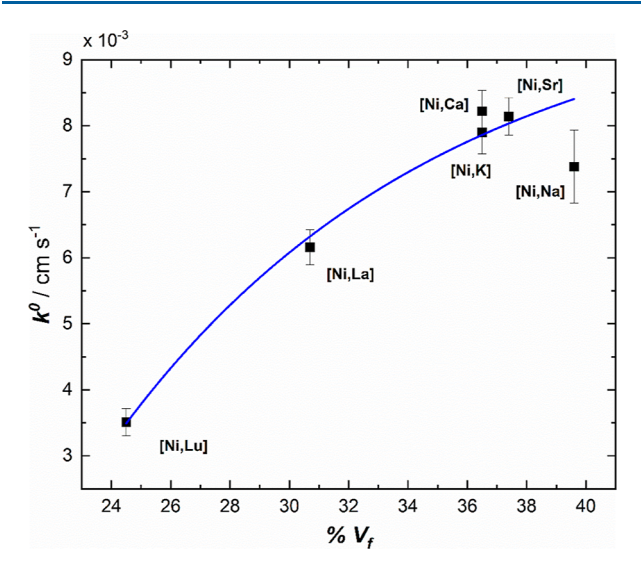


**Figure 11.** Scatter plot showing the relationship between %  $V_f$  and  $k^0$  of each relevant compound in the [Ni,M] family. The blue line is an exponential decay function and is intended primarily to guide the eye.

fastest ET rates are associated with the adducts of mono- and divalent cations, and slower rates associated with the adducts of trivalent cations. However, the diminishment of the ET rate for [Ni,La] is less significant than for [Ni,Lu], and simultaneously, the percent free volume is smaller for [Ni,Lu] than [Ni,La]. This correlation suggests that the impingement of the triflate counteranions into the microenvironment of the nickel center along with related structural changes in the macrocyclic ligand driven by incorporation of the trivalent cations results in the diminished ET rate for these species.

As presented above, [Ni,K] exists in the solid state as a dimer composed of two of the as-synthesized heterobimetallic species. All evidence suggests that the association between the heterobimetallic species is weak, meaning that the complex behaves as a free monomeric [Ni,K] species in solution. To provide support for this conclusion in the context of the SambVca analysis and consideration of ET rates, we carried out a buried volume determination with SambVca using the coordinates of the full dimeric species found in the solid state. The results show, as expected, that the percent free volume (%  $V_{\rm f}$ ) is much lower in the case of the dimeric species than the monomer (23.4% vs 36.5%, respectively; see Figures S135 and S136 for full comparison of data). When the %  $V_f$  of the dimeric [Ni,K] complex is used as the descriptor for ET rate  $(k^0)$ , the behavior does not obey the trend followed by all the six other heterobimetallic complexes (see Figure \$134). Thus, as the interactions holding the dimeric species together in the solid state can be concluded from the XRD analysis (vide supra) to be quite weak, we conclude that [Ni,K] behaves as a monomer in solution (see pp. \$59-\$60 for details). This analysis underscores the sensitivity of buried volume analysis to the solid-state structural data and reinforces the interpretations regarding the ET rates.

The modest value of  $k^0$  measured for [Ni,Y] is in accord with the structural data regarding impingement of triflate atoms into the nickel microenvironment for the other trivalent cation adducts. Although no structure of [Ni,Y] from XRD is available, the relevant ionic radii of La<sup>3+</sup> (CN = 10), Y<sup>3+</sup> (CN = 9), and Lu<sup>3+</sup> (CN = 9) decrease in a known order: 1.27, 1.08,

and 1.03 Å.<sup>21</sup> Similarly, the  $k^0$  values from the analysis decrease monotonically in the same order:  $6.2 \pm 0.3$ ,  $3.7 \pm 0.2$ , and  $3.5 \pm 0.2$  cm s<sup>-1</sup>. From the relationship shown in Figure 2, we could anticipate that incorporation of Y<sup>3+</sup> would lead to a Ni··· Y separation with a value intermediate between La<sup>3+</sup> and Lu<sup>3+</sup>. Thus, the data for [Ni,Y] lie along the trend measured in the free volume analysis. The ionic radius value for Y<sup>3+</sup> is intermediate between La<sup>3+</sup> and Lu<sup>3+</sup>, and the  $k^0$  value is also intermediate (see Figure S141). We thus conclude that the measured modest decrease in the ET is correlated with a decrease in solvent/electrolyte-exposed free volume in the adducts of the triflate salts of the trivalent cations.

**Topological Analysis of Analogous Palladium Complexes.** Our group previously reported the synthesis, structural characterization, and electrochemical properties of a family of heterobimetallic palladium(II) complexes. As this work involved the  $\mathbf{L_{salmen}}$  ligand platform that was also utilized here and the palladium complexes incorporated a similar range of metal triflate salts, we anticipated that the trends observed in the  $W_f$  and  $W_f$  studies reported here might be apparent in this older system as well. Indeed, the solid-state data for the  $W_f$  and  $W_f$  series show similar relationships between the  $W_f$  values of the aqua complexes corresponding to the incorporated secondary metal cations and the  $W_f$  about  $W_f$ 

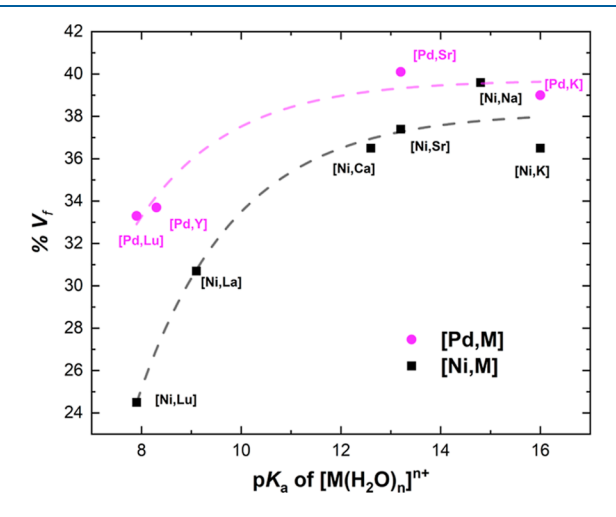


Figure 12. Plot showing the relationship between %  $V_{\rm f}$  and the p $K_{\rm a}$  values of the aqua complexes of the corresponding secondary cations  ${\bf M}^{\rm n+}$ . The structures of the complexes in the [Pd,M] series were previously reported in ref 9. The dashed lines are empirical exponential decay functions and are intended only to guide the eye.

attributable to the smaller ionic radius of Ni(II), 0.49 Å, in comparison to that of Pd(II), 0.64 Å.  $^{21}$  In both families of complexes, the triflate counteranions associated with trivalent cations impinge into the coordination spheres of the Group 10 metals, which are otherwise mostly unoccupied on the basis of %  $V_{\rm f}$  results for the adducts of divalent and monovalent cations (see Figures S131 and S132 and Table S6). The M'···M distance (M' = Ni or Pd) shows similar linear dependences on the ionic radius of M in both systems, albeit shifted to higher values for the Pd systems (see Figure S137). Unfortunately, the electrochemical behaviors for the [Pd,M] series were found be completely irreversible in all cases, precluding determination of  $k^0$  values. However, we do note that the reduction waves for the species incorporating trivalent cations were

broadened in comparison to those for the other derivatives, implying diminished ET kinetics for those cases (see  $\delta_{pc}$  values in Table S6). Thus, we conclude that the [Pd,M] and [Ni,M] systems show notable topological similarities that are likely driven by the use of triflate salts and the  $L_{salmen}$  ligand system in both cases.

Delineation of Possible Influences on the Correlation between ET Rate and Free Volume. The Marcus model of ET suggests several key physical parameters ( $\nu_N$ ,  $\kappa_E$ ,  $\lambda_{inner}$ , and  $\lambda_{\text{outer}}$ ) that could be impacted by the free volume changes about the nickel centers in the heterobimetallic complexes and lead to modulated ET rates. Among these, we anticipate that the nuclear frequency factor  $\nu_{\rm N}$  is unlikely to be changing significantly across our series of complexes, considering that the complexes' diffusion coefficients are all similar and the experiments to measure k0 were carried out with virtually identical conditions in each case.  $\lambda_{inner}$  could take on unique values for each complex, however, especially considering the observation of ligand radical character for the adducts of more strongly Lewis acidic cations.  $\lambda_{\text{outer}}$  could also depend on the identity of the incorporated cation, particularly if the association of the triflate anions with the complexes changes upon reduction to an extent depending on the cation identity.

We anticipate that the measured correlation between %  $V_{\rm f}$ and  $k^0$  suggests that the solid-state structures are relevant to the forms of the complexes adopted in solution. On the one hand, the impingement of the chemically inert and highly covalent C-F bonds of the triflate anions into the secondary coordination sphere of nickel could be associated with a decrease in  $\lambda_{\text{outer}}$ . We hypothesize that this could be the case because outer-sphere reorganization energy decreases in lower polarity solvents, <sup>57–60</sup> and thus, such behavior here could drive an increase in  $k^0$  upon impingement of the C-F moieties. However, this must be a minor effect, if present at all, considering that the measured  $k^0$  values decrease upon impingement of the C-F moieties. On the other hand, blocking of the nickel microenvironment with this steric bulk could result in a decrease in the electronic coupling between the molecular species and the electrode,  $H_{\rm electronic}$ , which would in turn result in a drop in the electronic transmission coefficient,  $\kappa_E$ . Thus, we speculate that decreased electronic coupling could be an important origin of the diminished ET kinetics measured for the species incorporating trivalent cations.

Additionally, we speculate that increased inner-sphere reorganization upon generation of the Ni(I) oxidation state for the trivalent cation adducts could also impact the kinetics, although the insight into this possibility comes from the structures of the Ni(II) complexes. As Ni(I) would be larger than Ni(II), if the O and N atoms of the salen-like  $[N_2, O_2]$ core are constrained to have a more or less fixed separation (sensible considering the macrocyclic nature of the complexes), the Ni center could be predicted to move out of the plane containing the  $[N_2, O_2]$  core upon reduction. This could cause the macrocycle to open up, upon reduction, across the O1···O2 separation that is a shared polyhedral edge with the secondary metal cations. Opening of this edge could induce considerable ligand movement, and in the case of the trivalent cations, there are three triflates that could move instead of the one or two in the adducts of monovalent or divalent cations. As any rearrangement in the trivalent cations' coordination spheres markedly affects %  $V_{\rm f}$ , it could be anticipated that the Ni(I) adducts of the trivalent cations would have significant

redox-induced structural deformations that would drive diminished ET kinetics through increased inner-sphere reorganization penalties, unlike the EDTA-encapsulated chromium centers studied in the reference from Bard that has guided our overall interpretations.  $^{51}$  Ni(I), owing to its likely tendency to move out of the macrocyclic plane, could also be more likely to interact than Ni(II) with the nearby triflate-derived O and F atoms above and below the macrocyclic plane for the trivalent adducts. In such a case, the lengthening Ni–O $_{\rm phen}$  bonds could drive shorter M–O $_{\rm phen}$  interactions, helping to facilitate further movement of the triflate anions toward the nascent Ni(I) center. Consequently, we speculate that increased  $\lambda_{\rm inner}$  values for the adducts of the trivalent cations could also contribute to the diminished kinetics for these species.

### DISCUSSION

The topological maps and buried volume analysis carried out with the SambVca webtool have provided quantitative data demonstrating that the impingement of the triflate counteranions associated with the trivalent cations into the secondary coordination sphere of the nickel center is correlated with diminished ET rates. SambVca is a broadly useful tool in structural studies of inorganic and organometallic systems, offering the ability to generate the maps and quantitative buried volume analyses from the Cartesian coordinates available from single-crystal XRD analysis or computational studies.<sup>55</sup> Utilization of SambVca here was inspired by the use of the webtool for applications in studies of catalysis, where it has been applied to understand how substrates might approach metal centers. 55,61 We note here that although we are aware of use of SambVca for applications in design of ligands for catalysis and correlations of product yields with steric parameters, 2,62 we are not aware of any prior study that has used topological mapping to study the possible origins of modulated ET kinetics. We anticipate that this approach could be useful in other studies of multimetallic complexes because redox behavior is often a consideration in such systems. Significant work from recent years has focused on the development of multimetallic catalysts and materials which rely on ET events to accomplish their designated functions; for example, multimetallic species have emerged as appealing catalysts for oxidation reactions, 63 model complexes for enzyme active sites, 3,64 and motifs for influencing the structural<sup>65</sup> and redox properties of the actinides.<sup>8,66</sup>

Along this line, Fukuzumi and co-workers presented one particularly relevant study of how incorporation of secondary metal cations could be used to modulate the driving force for ET in an oxygen-powered system for C-H bond functionalization; in their system, the kinetics of ET (and by extension, reaction turnover) were governed by the reduction potential of a key heterobimetallic species which underwent chemical reduction by an exogeneous equivalent of decamethylferrocene to trigger reactivity. Here, rather than using secondary metal cations to modulate the driving force for ET, we have identified a possible role for the secondary metal cations in governing the reorganization energy associated with a particular redox manifold. The mechanism underlying a role for secondary cations in driving increased reorganization energy penalties was not explicitly described in the work of Fukuzumi and co-workers, but the appearance of some of the data in these authors' report suggests that such an effect could also be operative in their system. Specifically, points on their

Marcus-like curve of reaction kinetics versus estimated thermodynamic driving force for the key reduction reaction show that the reorganization energy for trivalent cation adducts was apparently greater by about 340 meV compared to the value associated with mono- and divalent adducts (2.66 vs 2.32 eV). Although this difference has not been explored to date, the results offer preliminary possibilities that could correspond to a mechanistic origin of the effect. The authors utilized triflate salts in their work, as we have here. Thus, we anticipate that there could be a unique tendency for triflate salts of trivalent cations to engender decreased ET kinetics owing to their simultaneous tendency to both promote high coordination numbers and to display high steric demands. This could be due to increased reorganization energy or decreased electronic coupling with reaction partners. Exploration of counteranion-dependent behavior is thus underway in our laboratory at this time to make progress on understanding these effects in greater detail.

For both the [Ni,M] and [Pd,M] complexes, the first coordination spheres of the Group 10 metal cores do not show significant structural perturbations upon incorporation of the secondary metal cations. This observation applies to the tight range of Ni-O<sub>phen</sub> and Ni-N<sub>imine</sub> distances (see Figures S114 and S118) in the [Ni,M] series, as well as the uniformly low values of the  $\tau_4$  geometry index for [Ni] and all the heterobimetallic complexes. Our prior report indicated similar properties for the [Pd,M] series.9 Contrasting with these behaviors, the structural properties of the vanadyl (VO<sup>2+</sup>) complexes of the L<sub>salmen</sub> ligand vary more dramatically; the V-O<sub>phen</sub> distances were elongated, while the V-O<sub>oxo</sub> distances were contracted along the series [VO] - [VO,Na] -[VO,Ca]. We anticipate that these disparate findings may be attributable to greater structural degrees of freedom associated with the vanadyl complexes; the vanadium center sits above the plane of the macrocyclic ligand owing to its square pyramidal geometry, and compensation for diminished phenoxide donor power can apparently come from enhanced donation from the oxo group. Here, the nickel stays firmly in its square-planar geometry and bond distances do not change; this rigidity is a hallmark of the [Ni,M] series and its covalent Ni-L bonds. Investigation of the structures of the reduced species could shed light on the question of whether this apparent structural rigidity is translated to the lower valent forms of the complexes.

In a recent work with a family of high coordination number cerium(III) complexes (CN = 8), we identified that cationcation repulsion across heterometallic cores should be considered when interpreting the behavior of heterobimetallic complexes that feature bridging ligands.<sup>40</sup> Cation-cation repulsion of a Coulombic nature was observable between  $Ce^{3+}$  and  $M^{n+}$  centers, a feature attributed to the consideration that the electrostatic interactions which influence  $pK_a$  values involve  $\mathbf{M}^{n+}$  complexes of neutral  $H_2O$  or monoanionic hydroxide only, rather than multiple metal centers with intrinsic positive charges. In the case of the [Ni,M] complexes, this cation-cation repulsion does not appear to be as significant, likely because of the expected strong(er) Ni-O<sub>phenoxide</sub> bonding. The results of a deconvolution analysis (see pp. S84-S87) to examine the approach of the secondary cations to the covalent nickel core suggest that cation-cation repulsion only mildly affects interpretation of data in this system as a function of the  $pK_a$  values. In particular, the distance defined as "a" in the analysis (between the centroid of O1 and O2 and the nickel metal center; see Figure S122) suggests that cation-cation repulsion could slightly elongate the distance when stronger Lewis acids approach the nickel center, resulting in enhanced repulsion and deviation from what would otherwise be linear dependences of parameters on Lewis acidity. Similar analysis using ratios of Mn+ charge and ionic radius also confirm the presence of vestiges of cationcation repulsion in the acidity-driven effects (see Figures S125 and S126). The conceptually related anion-anion repulsion between phenoxide O atoms (O1 and O2) is apparently minimal, however, as a plot of this distance vs Mn+ ionic radius confirms a strong nonlinear correlation (see Figure S120) in accord with a similarly well correlated tightening of the O1-Ni–O2 angle (defined as  $\theta$ ; see Figure S124). Examination of the O1···O2 distance as a function of p $K_3$  (see Figure S121) returns a corresponding plot, with the smaller cations associated with smaller-than-predicted interatomic separations; this is attributable to the effect of cation-anion attraction between the highly Lewis acidic cations and the anionic phenoxide groups themselves. Considering all these features, we anticipate that the successful interpretation of "Lewis acid" dependent tuning effects as a function of the pKa values is a result of correlations of the  $pK_a$  values with cation charge, radius, and electronegativity as outlined previously by Wulfsberg. 19

Triflate appears to be uniquely suited to driving structural changes in the [Ni,M] complexes. The charge, size, and ability of triflate to form bridging interactions contribute to changes in the measured %  $V_f$  about nickel and could also be related to formation of the pseudo-octahedral O···Ni···F interactions. However, we note that triflate salts were selected for use here due to their high solubility, 17,18 enabling systematic studies and overcoming the very likely limited solubility of less sterically demanding salts featuring counteranions such as perchlorate. However, structurally simpler tetrahedral monoanions or dianions like perchlorate, sulfate, or phosphate should be considered for use in place of triflate in the context of these findings. We anticipate that these less sterically demanding anions would impinge to a lesser extent into the nickel microenvironment upon adduct formation. Fewer anions would be required to neutralize charge if divalent or trivalent anions were used, and this would also result in decreased steric bulk about nickel as well. Thus, if faster ET is desired, substitution of triflate for another smaller or more highly charged anion could be valuable. The formation of sterically congested coordination spheres is, as we have shown, driven partially by use of the triflate counteranions; this is supported by the structures from XRD, in that none show bound solvent, implying that triflates prefer to bind to the metal cations and to adopt bidentate configurations when space on the cations' coordination spheres remains rather than allowing solvent binding. Examining  $k^0$  as a function of ionic radius (see Figure S141) confirms this to be the case, as the  $k^0$  values for the divalent and trivalent cations having coordination numbers (CN) greater than or equal to nine and featuring two or more bound triflate counteranions (Sr<sup>2+</sup>, La<sup>3+</sup>, Y<sup>3+</sup>, and Lu<sup>3+</sup>) are essentially linearly dependent on the ionic radii values for the secondary cations, echoing the trend in cation position shown in Figure 2. [Ni,K] and [Ni,Sr] retain fast ET behavior despite the high CN of Mn+ because steric crowding about Ni is more modest in these cases than in the adducts of the trivalent cations.

In light of all these observations, use of tailored heteroditopic ligands for binding two or more metal cations can be confidently concluded to aid in the observation of structural and behavioral trends driven by exchange of one metal. This could be because ligands of the sort used by our group and others (multidentate chelates or macrocycles) are less flexible and impose restrictions on metal coordination numbers and geometries. In the work presented here, this restrictive nature has been shown to drive impingement of triflate moieties into the secondary coordination sphere of redox-active nickel, a structural phenomenon that appears to be correlated with diminished heterogeneous ET rates by impacting inner-sphere reorganization, electronic coupling with the electrode, or both. The structural effect is a result of both the demanding properties of the triflate salts of the trivalent cations as well as the structure of the macrocyclic ligand; the ligand drives a lateral movement of the cations and their triflates that depends on ionic radius, thus taking what would conventionally be a three-dimensional electrostatic effect and constraining it by vectorization into the approximately two-dimensional plane defined by the L<sub>salmen</sub> ligand and along the Ni···M vector. In other words, in these complexes, the [O-Ni-O] group is effectively like a large, rigid, and redox-active carboxyl group, and the cationic M species, along with their triflate counteranions to some extent, move in and out along the Ni...M vector depending on their ionic radii values. This work thus highlights this unique role of macrocyclic ligands in influencing ET behavior, suggesting new opportunities for rational control through structural effects. We anticipate that an appealing direction for future work could be examination of ligand variations that take into account tunable degrees of freedom, an approach that could directly examine influences on the vectorization of cation-induced effects and afford new insights into parameterization of these effects.

# CONCLUSIONS

In this work, a series of Ni-based macrocyclic and heterobimetallic complexes incorporating mono-, di-, and trivalent secondary metals (M) were prepared. The solidstate structures of the complexes reveal that the Ni···M distance is driven by the ionic radius of the secondary metal cations and that steric crowding about the Ni(II) ion by associated triflate counteranions increases when incorporating trivalent secondary cations. Heterogeneous ET is slowest for the complexes incorporating trivalent metal cations, and a topological analysis with the SambVca webtool confirmed a relationship between %  $V_f$  about nickel and  $k^0$ . Taken together, these results highlight the unique role that cations with high CN and high charge density can play in tuning of heterobimetallic systems. As these studies imply that complexes incorporating cations associated with more weakly coordinating counteranions could be anticipated to display both faster ET kinetics and even greater "tuning power" from the incorporated cations, investigations along this line are now underway in our laboratory.

### EXPERIMENTAL SECTION

**General Considerations.** All manipulations were carried out in dry  $N_2$ -filled gloveboxes (Vacuum Atmospheres Co., Hawthorne, CA) or under an  $N_2$  atmosphere using standard Schlenk techniques unless otherwise noted. All solvents were of commercial grade and dried over activated alumina using a PPT Glass Contour (Nashua, NH) solvent purification system prior to use and were stored over molecular sieves.

All chemicals were purchased from major commercial suppliers and used as received or after extensive drying. 2,3-Dihydroxybenzaldehyde was sublimed in vacuo before use. CD<sub>3</sub>CN was purchased from Cambridge Isotope Laboratories and dried over 3 Å molecular sieves.  $^1\mathrm{H},~^{13}\mathrm{C},~$  and  $^{19}\mathrm{F}$  NMR spectra were collected on 400 and 500 MHz Bruker spectrometers and referenced to the residual protio-solvent signal in the case of  $^1\mathrm{H}$  and  $^{13}\mathrm{C}.~^{19}\mathrm{F}$  NMR spectra were referenced and reported relative to CCl<sub>3</sub>F as an external standard following the recommended scale based on the ratios of absolute frequencies (Ξ). Chemical shifts (δ) are reported in units of ppm, and coupling constants (*J*) are reported in Hz. NMR spectra are given in the Supporting Information (Figures S1–S39). Electronic absorption spectra were collected with an Ocean Optics Flame spectrometer, in a 1 cm path length quartz cuvette. Details regarding the use of the SambVca 2.1 webtool are given in the Supporting Information (p. S88).

Electrochemistry. Electrochemical experiments were carried out in a N2-filled glovebox in dry, degassed CH3CN. 0.10 M Tetra(nbutylammonium) hexafluorophosphate ([nBu<sub>4</sub>N] + [PF<sub>6</sub>]-), Sigma-Aldrich, of electrochemical grade served as the supporting electrolyte. Measurements were made with a Gamry Reference 600+ Potentiostat/Galvanostat using a standard three-electrode configuration. The working electrode was the basal plane of highly oriented pyrolytic graphite (HOPG) (GraphiteStore.com, Buffalo Grove, Ill.; surface area: 0.09 cm<sup>2</sup>), the counter electrode was a platinum wire (Kurt J. Lesker, Jefferson Hills, PA; 99.99%, 0.5 mm diameter), and a silver wire immersed in the electrolyte served as a pseudoreference electrode (CH Instruments). The reference was separated from the working solution by a Vycor frit (Bioanalytical Systems, Inc.). Ferrocene (Sigma-Aldrich; twice-sublimed) was added to the electrolyte solution prior to the beginning of each experiment; the midpoint potential of the ferrocenium/ferrocene couple (denoted as Fc<sup>+/0</sup>) served as an internal standard for comparison of the recorded potentials. Concentrations of analyte for cyclic voltammetry were ca. 2 mM unless otherwise noted. Compensation for solution resistance (measured by impedance spectroscopy to be small, ca. 110–150  $\Omega$ ) was not carried out for any of the data presented here; based on preliminary comparisons, the data quality was higher without applying

**Synthesis and Characterization.** Caution! Sodium hydride (NaH) is a flammable solid. Hydrogen gas is released upon contact of NaH with water, and the gas may ignite spontaneously. NaH causes severe skin burns and eye damage. Store in a dry place and in a closed container with a corrosion-resistant liner. Wear protective gloves, a suitable laboratory coat, and eye protection when using NaH.

Synthesis of 3,3'-(3,6-Dioxaoctane-1,8-diyldioxy)bis(2-hydroxybenzaldehyde). Under an inert atmosphere of nitrogen, a dry Schlenk flask was loaded with 2,3-dihydroxybenzaldehyde (1.2 g, 8.85 mmol) dissolved in 15 mL of dry THF. This solution was transferred using a syringe to a suspension of NaH (0.47 g, 19.5 mmol) in 5 mL of dry THF under N<sub>2</sub> over a period of 1 h. The temperature was kept below 25 °C. The color change to bright yellow indicates the formation of disodium salt of 2,3-dihydroxybenzaldehyde. The ice bath was removed after addition, and the mixture was stirred for 1 h at room temperature. Under a positive flow of N2, triethylene glycol ditosylate (2.03 g, 4.42 mmol) dissolved in 25 mL of dry THF was added to the yellow mixture in a single aliquot using a syringe. The resulting mixture was then stirred for 60 h under a static N<sub>2</sub> atmosphere and 45 °C. Addition of 80 mL of water resulted in a dark brown solution that was extracted twice with CHCl3. The aqueous layer was treated with 6 M HCl until the pH of the mixture was 1. This mixture was then extracted with three portions of CHCl<sub>3</sub>. The combined organic layers were washed with 1 M HCl and dried over anhydrous MgSO<sub>4</sub>. Evaporation of solvent yielded a pale-yellow solid which was used without any further purification. Yield: 84% (1.46 g). Spectroscopic characterization by <sup>1</sup>H NMR provided spectra that were virtually identical to those obtained in a prior report.<sup>2</sup>

**Synthesis of [Ni,Ba].** To a three-necked flask of a refluxing solution of Ba(OTf)2 (1.64 g, 3.78 mmol) dissolved in 250 mL of CH<sub>3</sub>OH (0.015 M), 1 equiv of 3,3'-(3,6-dioxaoctane-1,8-diyldioxy)-

bis(2-hydroxybenzaldehyde) (1.46 g, 3.73 mmol) in 65 mL of THF (0.06 M) was slowly added. One equiv of 1,2-diamino-2-methylpropane (0.336 g, 3.81 mmol) in 65 mL of CH<sub>3</sub>OH (0.059 M) was added dropwise over a period of 5 h. The reaction mixture was refluxed for 30 min. 1 equiv of Ni(OAc)<sub>2</sub>\*4(H<sub>2</sub>O) (0.94 g, 3.77 mmol) was added, and the solution was allowed to reflux for 10 more minutes before being left to cool to room temperature overnight. The solution was then evaporated on the rotary evaporator until concentrated. Ether was used to wash and titrate the solution and resulting solid until a brown powder formed. Spectroscopic characterization by  $^1\mathrm{H}$  NMR provided spectra that were virtually identical to those obtained in a prior report.  $^{23}$ 

Synthesis of [Ni]. An excess of guanidinium sulfate (4.06 g, 18.6 mmol) dissolved in 250 mL of water was added to a suspension of [Ni,Ba] (1.16 g, 1.24 mmol) in 50 mL of CHCl<sub>3</sub> under stirring for at least 4 days. The organic layer was separated, and the water layer was washed with CHCl<sub>3</sub> twice or until the CHCl<sub>3</sub> was clear. CHCl<sub>3</sub> that contains the product was then dried on a rotary evaporator until concentrated. The concentrated solution was then washed with cold hexanes to precipitate the product in the form of a brown, fine powder. This powder was then collected by vacuum filtering the solution with a medium frit. Spectroscopic characterization by <sup>1</sup>H NMR provided spectra that were virtually identical to those obtained in a prior report.<sup>23</sup>

[Ni]. Yield: 84.4%.  $^{1}$ H NMR (500 MHz, CD<sub>3</sub>CN):  $\delta$  (ppm): 7.60 (s, 1H, H3), 7.59 (s, 1H, H3), 6.88 (d,  $^{3}J_{\rm H,H}$  = 8.05, 1H, H4), 6.81 (d,  $^{3}J_{\rm H,H}$  = 8.00, 1H, H4), 6.71 (d,  $^{3}J_{\rm H,H}$  = 7.50, 2H, H6), 6.46 (t,  $^{3}J_{\rm H,H}$  = 7.10, 1H, H5), 6.45 (t,  $^{3}J_{\rm H,H}$  = 7.55, 1H, H5), 3.95 (m, 4H, H7), 3.72 (m, 4H, H8), 3.65 (s, 4H, H9), 3.24 (s, 2H, H2), 1.46 (s, 6H, H1).  $^{13}$ C { $^{1}$ H} NMR (126 MHz, CD<sub>3</sub>CN):  $\delta$  (ppm): 163.29, 160.20, 156.80, 156.15, 151.33, 151.23, 125.27, 124.69, 121.47, 121.27, 114.60, 114.58, 113.75, 113.71, 71.58, 70.48, 69.60, 67.94, 67.92, 66.71, 25.88. Cyclic voltammetry (0.1 M [nBu<sub>4</sub>N]<sup>+</sup>[PF<sub>6</sub>]<sup>-</sup> in CH<sub>3</sub>CN):  $E_{1/2}$  = -2.129 V vs Fc<sup>+/0</sup>. Electronic absorption spectrum in CH<sub>3</sub>CN (M<sup>-1</sup> cm<sup>-1</sup>): 420 (5398), 550 (103) nm.

Synthesis of [Ni,M] Heterobimetallic Complexes. Under an inert atmosphere, a heterogeneous solution of [Ni] in CH<sub>3</sub>CN was added to 1 equiv of corresponding metal salt solution in CH<sub>3</sub>CN and stirred for 30 min. The reaction is accompanied by a color change of the brown solution of [Ni] to a red or orange-colored solution depending on the concentration. The solvent was removed in vacuo to give the desired product. Yields were typically near quantitative (vide infra). Crystals suitable for XRD were obtained by vapor diffusion of diethyl ether into a CH<sub>3</sub>CN solution of the [Ni,M] complexes for [Ni,K], [Ni,Na], and [Ni,Sr]. Crystals of [Ni,Ca] suitable for XRD were obtained by vapor diffusion of CH<sub>2</sub>Cl<sub>2</sub> into a CH<sub>3</sub>OH solution stored outside the glovebox. Crystals of [Ni,La] and [Ni,Lu] suitable for XRD were obtained by vapor diffusion of CH<sub>2</sub>Cl<sub>2</sub> into a CH<sub>3</sub>CN solution inside of the glovebox.

Elemental analyses for all bimetallic complexes were performed by Midwest Microlab, Inc. (Indianapolis, IN).

[Ni,K]. Yield: 96%. <sup>1</sup>H NMR (500 MHz, CD<sub>3</sub>CN):  $\delta$  (ppm): 7.65 (s, 2H, H3), 6.98 (d,  ${}^{3}J_{\text{H,H}} = 8.05$ , 1H, H4), 6.91 (d,  ${}^{3}J_{\text{H,H}} = 8.00$ , 1H, H4), 6.85 (d,  ${}^{3}J_{\text{H,H}} = 7.70$ , 2H, H6), 6.59 (t,  ${}^{3}J_{\text{H,H}} = 7.65$ , 1H, H5), 6.58 (t,  ${}^{3}J_{\text{H,H}} = 7.55$ , 1H, H5), 4.06 (m, 4H, H7), 3.83 (m, 4H, H8), 3.73 (s, 4H, H9), 3.28 (s, 2H, H2), 1.48 (s, 6H, H1). <sup>13</sup>C { }^{1}H } NMR (126 MHz, CD<sub>3</sub>CN):  $\delta$  (ppm): 164.17, 161.09, 154.58, 153.93, 150.19, 150.09, 126.24, 125.67, 121.51, 121.33, 115.85, 115.82, 114.43, 71.50, 70.29, 70.27, 69.13, 67.77, 67.34, 25.76. <sup>19</sup>F NMR (471 MHz, CD<sub>3</sub>CN):  $\delta$  — 80.19. Anal. Calcd for C<sub>25</sub>H<sub>28</sub>F<sub>3</sub>KN<sub>2</sub>O<sub>9</sub>SNi ([Ni,K]): C 43.68, H 4.08, N 4.11. Found: C 43.37, H 4.28, N 4.07. Cyclic voltammetry (0.1 M [nBu<sub>4</sub>N]<sup>+</sup>[PF<sub>6</sub>] in CH<sub>3</sub>CN):  $E_{1/2}$  = -1.949 V vs Fc<sup>+/0</sup>. Electronic absorption spectrum in CH<sub>3</sub>CN (M<sup>-1</sup> cm<sup>-1</sup>): 409(4323). 545 (104) nm.

cm<sup>-1</sup>): 409(4323), 545 (104) nm. [Ni,Na]. Yield: 98%.  $^{1}$ H NMR (500 MHz, CD<sub>3</sub>CN):  $\delta$  (ppm): 7.69 (s, 2H, H3), 7.00 (d,  $^{3}$ J<sub>H,H</sub> = 8.05, 1H, H4), 6.93 (d,  $^{3}$ J<sub>H,H</sub> = 8.00, 1H, H4), 6.88 (d,  $^{3}$ J<sub>H,H</sub> = 7.75, 2H, H6), 6.61 (t,  $^{3}$ J<sub>H,H</sub> = 7.80, 1H, H5), 6.60 (t,  $^{3}$ J<sub>H,H</sub> = 7.70, 1H, H5), 4.06 (m, 4H, H7), 3.82 (m, 4H, H8), 3.70 (s, 4H, H9), 3.32 (s, 2H, H2), 1.48 (s, 6H, H1).  $^{13}$ C { $^{1}$ H} NMR (126 MHz, CD<sub>3</sub>CN):  $\delta$  (ppm): 163.73, 160.71, 153.83, 153.19,

149.54, 149.43, 125.74, 125.19, 120.99, 120.80, 115.60, 115.57, 114.37, 114.35, 70.93, 69.54, 69.51, 68.16, 67.44, 66.91, 25.36.  $^{19}\mathrm{F}$  NMR (376 MHz, CD\_3CN):  $\delta$  – 80.19. Anal. Calcd for C25H28F3NaN2O9SNi ([Ni,Na]): C 44.73, H 4.20, N 4.17. Found: C 43.97, H 4.38, N 4.45. Calcd for C25H28F3NaN2O9SNi + 0.5H2O: C 43.56, H 4.39, N 4.06. Water inclusion in the sample likely resulted from shipping, as these complexes are hygroscopic. Cyclic voltammetry (0.1 M [nBu4N]+[PF6] in CH3CN):  $E_{1/2} = -1.953$  V vs Fc+/0. Electronic absorption spectrum in CH3CN (M $^{-1}$  cm $^{-1}$ ): 406(4690), 549 (92) nm.

[Ni,Sr]. Yield: 98%.  $^1$ H NMR (500 MHz, CD<sub>3</sub>CN):  $\delta$  (ppm): 7.72 (s, 1H, H3), 7.71 (s, 1H, H3), 7.14 (d,  $^3J_{\rm H,H}$  = 8.00, 1H, H4), 7.06 (d,  $^3J_{\rm H,H}$  = 6.15, 1H, H4), 7.04 (d,  $^3J_{\rm H,H}$  = 7.00, 2H, H6), 6.77 (t,  $^3J_{\rm H,H}$  = 7.95, 1H, H5), 6.76 (t,  $^3J_{\rm H,H}$  = 7.95, 1H, H5), 4.25 (m, 4H, H7), 4.04 (m, 4H, H8), 3.90 (s, 4H, H9), 3.35 (s, 2H, H2), 1.51 (s, 6H, H1).  $^{13}$ C { $^1$ H} NMR (126 MHz, CD<sub>3</sub>CN):  $\delta$  (ppm): 165.19, 162.05, 151.28, 150.62, 148.95, 148.82, 127.51, 126.96, 121.34, 121.16, 117.74, 117.71, 115.78, 71.31, 70.93, 70.88, 69.20, 68.03, 25.57.  $^{19}$ F NMR (471 MHz, CD<sub>3</sub>CN):  $\delta$  — 80.09. Anal. Calcd for C<sub>26</sub>H<sub>28</sub>F<sub>6</sub>SrN<sub>2</sub>O<sub>12</sub>S<sub>2</sub>Ni ([Ni,Sr]): C 35.29, H 3.19, N 3.16. Found: C 34.41, H 3.36, N 3.09. Calcd For C<sub>26</sub>H<sub>28</sub>F<sub>6</sub>SrN<sub>2</sub>O<sub>12</sub>S<sub>2</sub>Ni + H<sub>2</sub>O: C 34.58, H 3.35, N 3.10. Water inclusion in the sample is due to the hygroscopic nature of the complex, as water is retained in  $^1$ H NMR even after overnight drying of the complex. Cyclic voltammetry (0.1 M [nBu<sub>4</sub>N]<sup>+</sup>[PF<sub>6</sub>]<sup>-</sup> in CH<sub>3</sub>CN):  $E_{1/2}$  = -1.684 V vs Fc<sup>+/0</sup>. Electronic absorption spectrum in CH<sub>3</sub>CN (M<sup>-1</sup> cm<sup>-1</sup>): 390 (4521), 540 (114) nm.

[Ni,Ca]. Yield: 96%. 1H NMR (500 MHz, CD<sub>3</sub>CN):  $\delta$  (ppm): 7.74 (s, 1H, H3), 7.73 (s, 1H, H3), 7.15 (d,  ${}^3J_{\rm H,H}$  = 8.00, 1H, H4), 7.07 (d,  ${}^3J_{\rm H,H}$  = 8.00, 1H, H4), 7.05 (d,  ${}^3J_{\rm H,H}$  = 7.85, 2H, H6), 6.79 (t,  ${}^3J_{\rm H,H}$  = 7.95, 1H, H5), 6.78 (t,  ${}^3J_{\rm H,H}$  = 7.90, 1H, H5), 4.25 (m, 4H, H7), 4.06 (m, 4H, H8), 3.94 (s, 4H, H9), 3.36 (s, 2H, H2), 1.52 (s, 6H, H1).  ${}^{13}$ C { $^{1}$ H} NMR (126 MHz, CD<sub>3</sub>CN):  $\delta$  (ppm): 165.05, 161.88, 150.65, 150.05, 148.69, 148.59, 127.35, 126.80, 121.17, 120.96, 117.98, 117.95, 115.86, 115.79, 71.07, 70.40, 68.63, 68.14, 68.03, 67.99, 25.53.  ${}^{19}$ F NMR (471 MHz, CD<sub>3</sub>CN):  $\delta$  — 80.14. Anal. Calcd for C<sub>26</sub>H<sub>28</sub>F<sub>6</sub>CaN<sub>2</sub>O<sub>12</sub>S<sub>2</sub>Ni ([Ni,Ca]): C 37.29, H 3.37, N 3.34. Found: C 37.55, H 3.59, N 3.15. Cyclic voltammetry (0.1 M [nBu<sub>4</sub>N]+[PF<sub>6</sub>]- in CH<sub>3</sub>CN):  $E_{1/2}$  = -1.682 V vs Fc<sup>+/0</sup>. Electronic absorption spectrum in CH<sub>3</sub>CN (M<sup>-1</sup> cm<sup>-1</sup>): 388 (5940), 539 (129)

[Ni,La]. Yield: 98%.  $^1$ H NMR (500 MHz, CD<sub>3</sub>CN):  $\delta$  (ppm): 8.23 (s, 1H, H3), 8.16 (s, 1H, H3), 7.26 (d,  $^3$ J<sub>H,H</sub> = 8.00, 1H, H4), 7.21 (d,  $^3$ J<sub>H,H</sub> = 8.00, 1H, H6), 7.18 (d,  $^3$ J<sub>H,H</sub> = 7.90, 2H, H4), 6.92 (t,  $^3$ J<sub>H,H</sub> = 7.30, 1H, H5), 6.91 (t,  $^3$ J<sub>H,H</sub> = 7.30, 1H, H5), 4.48 (m, 4H, H7), 4.21 (m, 4H, H8), 4.13 (s, 4H, H9), 3.42 (s, 2H, H2), 1.54 (s, 6H, H1).  $^{13}$ C { $^1$ H} NMR (126 MHz, CD<sub>3</sub>CN):  $\delta$  (ppm): 165.88, 162.36, 149.42, 149.32, 148.60, 147.96, 128.65, 128.14, 121.19, 121.00, 119.61, 119.59, 117.24, 72.23, 72.22, 70.61, 70.55, 69.59, 68.34, 25.33.  $^{19}$ F NMR (471 MHz, CD<sub>3</sub>CN):  $\delta$  - 79.94. Anal. Calcd for C<sub>27</sub>H<sub>28</sub>F<sub>9</sub>LaN<sub>2</sub>O<sub>15</sub>S<sub>3</sub>Ni ([Ni,La]): C 29.88, H 2.60, N 2.58. Found: C 29.63, H 2.85, N 2.50. Cyclic voltammetry (0.1 M [nBu<sub>4</sub>N]<sup>+</sup>[PF<sub>6</sub>]<sup>-</sup> in CH<sub>3</sub>CN):  $E_{1/2} = -1.423$  V vs Fc<sup>+/0</sup>. Electronic absorption spectrum in CH<sub>3</sub>CN (M<sup>-1</sup> cm<sup>-1</sup>): 370 (4576), 535 (87) nm.

[Ni,Y]. Yield: 97%.  $^{1}$ H NMR (500 MHz, CD<sub>3</sub>CN):  $\delta$  (ppm): 7.85 (s, 1H, H3), 7.83 (s, 1H, H3), 7.28 (d,  $^{3}J_{\rm H,H}$  = 8.00, 1H, H4), 7.20 (m, 1H, H6, H4), 6.95 (t,  $^{3}J_{\rm H,H}$  = 8.00, 1H, H5), 6.92 (t,  $^{3}J_{\rm H,H}$  = 8.00, 1H, H5), 4.51 (m, 4H, H7), 4.32 (m, 4H, H8), 4.22 (m, 4H, H9), 3.37 (s, 2H, H2), 1.55 (s, 6H, H1).  $^{13}$ C { $^{1}$ H} NMR (126 MHz, CD<sub>3</sub>CN):  $\delta$  (ppm): 165.39, 162.21, 147.98, 147.81, 147.73, 147.04, 128.25, 127.86, 121.34, 121.01, 120.04, 119.80, 117.21, 117.13, 71.83, 71.56, 71.24, 71.08, 70.42, 68.95, 68.70, 68.53, 25.24.  $^{19}$ F NMR (376 MHz, CD<sub>3</sub>CN):  $\delta$  — 80.06. Anal. Calcd for C<sub>27</sub>H<sub>28</sub>F<sub>9</sub>N<sub>2</sub>YO<sub>15</sub>S<sub>3</sub>Ni ([Ni,Y]): C 31.32, H 2.73, N 2.70. Found: C 29.08, H 2.91, N 2.61. Calcd for C<sub>27</sub>H<sub>28</sub>F<sub>9</sub>N<sub>2</sub>YO<sub>15</sub>S<sub>3</sub>Ni + CH<sub>2</sub>Cl<sub>2</sub>: C 28.95, H 2.70, N 2.50. CH<sub>2</sub>Cl<sub>2</sub> inclusion in the sample is likely due to the purification process of [Ni,Y], which provided a crystalline powder with the same process used for the crystallization of [Ni,La] and [Ni,Lu]. Cyclic voltammetry (0.1 M [nBu<sub>4</sub>N]<sup>+</sup>[PF<sub>6</sub>]<sup>-</sup> in CH<sub>3</sub>CN):  $E_{1/2}$  = -1.445 V

vs Fc $^{+/0}$ . Electronic absorption spectrum in CH $_3$ CN (M $^{-1}$  cm $^{-1}$ ): 378 (4275), 532 (118) nm.

[Ni,Lu]. Yield: 97%. <sup>1</sup>H NMR (500 MHz, CD<sub>3</sub>CN):  $\delta$  (ppm): 7.90 (s, 1H, H3), 7.88 (s, 1H, H3), 7.28 (d,  ${}^{3}J_{H,H} = 8.05$ , 1H, H4), 7.21 (m,  ${}^{3}J_{H,H} = 8.05$ , 2H, H6), 7.20 (d,  ${}^{3}J_{H,H} = 8.00$ , 1H, H4), 6.95 (t,  ${}^{3}J_{H,H}$  = 8.00, 1H, H5), 6.93 (t,  ${}^{3}J_{H,H}$  = 8.05, 1H, H5), 4.51 (m, 4H, H7), 4.31 (m, 4H, H8), 4.22 (s, 4H, H9), 3.40 (s, 2H, H2), 1.55 (s, 6H, H1).  $^{13}$ C  $\{^{1}$ H $\}$  NMR (126 MHz, CD<sub>3</sub>CN):  $\delta$  (ppm): 165.27, 162.16, 147.97, 147.82, 147.80, 147.14, 128.31, 127.92, 121.61, 121.29, 120.10, 119.89, 117.55, 117.45, 71.69, 71.53, 71.45, 71.40, 70.39, 68.95, 68.79, 68.57, 25.27.  $^{19}\mathrm{F}$  NMR (376 MHz, CD<sub>3</sub>CN):  $\delta$  – 80.05. Anal. Calcd for  $C_{27}H_{28}F_9N_2LuO_{15}S_3Ni$  ([Ni,Lu]): C 28.92, H 2.52, N 2.50. Found: C 27.87, H 2.84, N 2.83. Calcd for  $C_{27}H_{28}F_9N_2LuO_{15}S_3Ni + CH_2Cl_2 + 0.25 CH_3CN: C 28.14, H 2.59,$ N 2.55. CH<sub>2</sub>Cl<sub>2</sub> and CH<sub>3</sub>CN were likely included in the sample due to the crystallization method used to purify [Ni,Lu]. Cyclic voltammetry (0.1 M  $[nBu_4N]^+[PF_6]^-$  in CH<sub>3</sub>CN):  $E_{1/2} = -1.426$  V vs Fc<sup>+/0</sup>. Electronic absorption spectrum in CH<sub>3</sub>CN (M<sup>-1</sup> cm<sup>-1</sup>): 374 (4369), 532 (113) nm.

## ASSOCIATED CONTENT

## Supporting Information

The Supporting Information is available free of charge at https://pubs.acs.org/doi/10.1021/acs.inorgchem.4c00230.

NMR spectra; characterization data for the complexes reported in this work; electrochemical data and related analysis; and detailed information regarding the XRD analysis (PDF)

Cartesian coordinates for the XRD structures (XYZ)

## **Accession Codes**

CCDC 2283630-2283635 contain the supplementary crystallographic data for this paper. These data can be obtained free of charge via <a href="www.ccdc.cam.ac.uk/data\_request/cif">www.ccdc.cam.ac.uk/data\_request/cif</a>, or by emailing <a href="data\_request@ccdc.cam.ac.uk">data\_request/cif</a>, or by contacting The Cambridge Crystallographic Data Centre, 12 Union Road, Cambridge CB2 1EZ, UK; fax: +44 1223 336033.

# AUTHOR INFORMATION

## **Corresponding Author**

James D. Blakemore — Department of Chemistry, University of Kansas, Lawrence, Kansas 66045, United States; orcid.org/0000-0003-4172-7460; Phone: (785) 864-3019; Email: blakemore@ku.edu

# Authors

Joseph P. Karnes – Department of Chemistry, University of Kansas, Lawrence, Kansas 66045, United States

Amit Kumar — Department of Chemistry, University of Kansas, Lawrence, Kansas 66045, United States; Present Address: Heraeus Precious Metals, 15524 Carmenita Road, Santa Fe Springs, California 90670, United States; orcid.org/0000-0001-8704-5997

Julie A. Hopkins Leseberg – Department of Chemistry, University of Kansas, Lawrence, Kansas 66045, United States; Present Address: Research & Technology, Chevron Phillips Chemical, Kingwood, Texas 77339, United States

Victor W. Day – Department of Chemistry, University of Kansas, Lawrence, Kansas 66045, United States

Complete contact information is available at: https://pubs.acs.org/10.1021/acs.inorgchem.4c00230

#### **Author Contributions**

The manuscript was written through contributions of all authors. All authors have given approval to the final version of the manuscript.

#### **Notes**

The authors declare no competing financial interest.

### ACKNOWLEDGMENTS

This work was supported by the U.S. Department of Energy, Office of Science, Office of Basic Energy Sciences, through the Early Career Research Program (DE-SC0019169). J.P.K. was supported by a U.S. National Science Foundation Research Traineeship (NRT) at the University of Kansas (DGE-1922649). A preprint reflecting a preliminary version of the findings reported here was posted to a preprint server. <sup>67</sup>

## REFERENCES

- (1) Ramirez, B. L.; Lu, C. C. Rare-Earth Supported Nickel Catalysts for Alkyne Semihydrogenation: Chemo- and Regioselectivity Impacted by the Lewis Acidity and Size of the Support. *J. Am. Chem. Soc.* **2020**, *142*, 5396–5407.
- (2) Tran, T. V.; Karas, L. J.; Wu, J. I.; Do, L. H. Elucidating Secondary Metal Cation Effects on Nickel Olefin Polymerization Catalysts. *ACS Catal.* **2020**, *10*, 10760–10772.
- (3) Kanady, J. S.; Tsui, E. Y.; Day, M. W.; Agapie, T. Synthetic Model of the Mn<sub>3</sub>Ca Subsite of the Oxygen-Evolving Complex in Photosystem II. *Science* **2011**, 333, 733–736.
- (4) Devi, T.; Lee, Y.-M.; Nam, W.; Fukuzumi, S. Tuning Electron-Transfer Reactivity of a Chromium(III)—Superoxo Complex Enabled by Calcium Ion and Other Redox-Inactive Metal Ions. *J. Am. Chem. Soc.* **2020**, *142*, 365–372.
- (5) Kumar, A.; Lionetti, D.; Day, V. W.; Blakemore, J. D. Trivalent Lewis Acidic Cations Govern the Electronic Properties and Stability of Heterobimetallic Complexes of Nickel. *Chem.—Eur. J.* **2018**, *24*, 141–149.
- (6) Windorff, C. J.; Chen, G. P.; Cross, J. N.; Evans, W. J.; Furche, F.; Gaunt, A. J.; Janicke, M. T.; Kozimor, S. A.; Scott, B. L. Identification of the Formal + 2 Oxidation State of Plutonium: Synthesis and Characterization of  $\{Pu^{II}[C_5H_3(SiMe_3)_2]_3\}$ –. *J. Am. Chem. Soc.* **2017**, *139*, 3970–3973.
- (7) Ryan, A. J.; Ziller, J. W.; Evans, W. J. The importance of the counter-cation in reductive rare-earth metal chemistry: 18-crown-6 instead of 2,2,2-cryptand allows isolation of  $[Y^{II}(NR_2)_3]^{1-}$  and ynediolate and enediolate complexes from CO reactions. *Chem. Sci.* **2020**, *11*, 2006–2014.
- (8) Kumar, A.; Lionetti, D.; Day, V. W.; Blakemore, J. D. Redox-Inactive Metal Cations Modulate the Reduction Potential of the Uranyl Ion in Macrocyclic Complexes. *J. Am. Chem. Soc.* **2020**, *142*, 3032–3041.
- (9) Golwankar, R. R.; Kumar, A.; Day, V. W.; Blakemore, J. D. Revealing the Influence of Diverse Secondary Metal Cations on Redox-Active Palladium Complexes. *Chem.—Eur. J.* **2022**, 28, No. e202200344.
- (10) Dopp, C. M.; Golwankar, R. R.; Kelsey, S. R.; Douglas, J. T.; Erickson, A. N.; Oliver, A. G.; Day, C. S.; Day, V. W.; Blakemore, J. D. Vanadyl as a Spectroscopic Probe of Tunable Ligand Donor Strength in Bimetallic Complexes. *Inorg. Chem.* **2023**, *62*, 9827–9843.
- (11) (a) Deacy, A. C.; Moreby, E.; Phanopoulos, A.; Williams, C. K. Co(III)/Alkali-Metal(I) Heterodinuclear Catalysts for the Ring-Opening Copolymerization of CO<sub>2</sub> and Propylene Oxide. *J. Am. Chem. Soc.* **2020**, *142*, 19150–19160. (b) Lindeboom, W.; Fraser, D. A. X.; Durr, C. B.; Williams, C. K. Heterodinuclear Zn(II), Mg(II) or Co(III) with Na(I) Catalysts for Carbon Dioxide and Cyclohexene Oxide Ring Opening Copolymerizations. *Chem.—Eur. J.* **2021**, *27*, 12224–12231. (c) Diment, W. T.; Williams, C. K. Chain end-group selectivity using an organometallic Al(III)/K(I) ring-opening copolymerization catalyst delivers high molar mass, monodisperse

- polyesters. *Chem. Sci.* **2022**, *13*, 8543–8549. (d) Fiorentini, F.; Diment, W. T.; Deacy, A. C.; Kerr, R. W. F.; Faulkner, S.; Williams, C. K. Understanding catalytic synergy in dinuclear polymerization catalysts for sustainable polymers. *Nat. Commun.* **2023**, *14*, 4783. (e) Shellard, E. J. K.; Diment, W. T.; Resendiz-Lara, D. A.; Fiorentini, F.; Gregory, G. L.; Williams, C. K. Al(III)/K(I) Heterodinuclear Polymerization Catalysts Showing Fast Rates and High Selectivity for Polyester Polyols. *ACS Catal.* **2024**, *14*, 1363–1374.
- (12) Langley, S. K.; Le, C.; Ungur, L.; Moubaraki, B.; Abrahams, B. F.; Chibotaru, L. F.; Murray, K. S. Heterometallic 3d–4f Single-Molecule Magnets: Ligand and Metal Ion Influences on the Magnetic Relaxation. *Inorg. Chem.* **2015**, *54*, 3631–3642.
- (13) Reath, A. H.; Ziller, J. W.; Tsay, C.; Ryan, A. J.; Yang, J. Y. Redox Potential and Electronic Structure Effects of Proximal Nonredox Active Cations in Cobalt Schiff Base Complexes. *Inorg. Chem.* **2017**, *56*, 3713–3718.
- (14) Kang, K.; Fuller, J.; Reath, A. H.; Ziller, J. W.; Alexandrova, A. N.; Yang, J. Y. Installation of internal electric fields by non-redox active cations in transition metal complexes. *Chem. Sci.* **2019**, *10*, 10135–10142.
- (15) Truter, M. R. Structures of organic complexes with alkali metal ions. *Struct. Bonding (Berlin)* **1973**, *16*, 71–111.
- (16) Perrin, D. D. Ionisation Constants of Inorganic Acids and Bases in Aqueous Solution; Pergamon Press: New York, 1982.
- (17) Kumar, A.; Blakemore, J. D. On the Use of Aqueous Metal-Aqua pKa Values as a Descriptor of Lewis Acidity. *Inorg. Chem.* **2021**, 60, 1107–1115.
- (18) Golwankar, R. R.; Curry, T. D.; Paranjothi, C. J.; Blakemore, J. D. Molecular Influences on the Quantification of Lewis Acidity with Phosphine Oxide Probes. *Inorg. Chem.* **2023**, *62*, 9765–9780.
- (19) Wulfsberg, G. Principles of Descriptive Inorganic Chemistry; University Science Books: Mill Valley, Calif., 1991, pp 27–31.
- (20) Shannon, R. D.; Prewitt, C. T. Revised values of effective ionic radii. *Acta Crystallogr.* **1970**, *26*, 1046–1048.
- (21) Shannon, R. D. Revised effective ionic radii and systematic studies of interatomic distances in halides and chalcogenides. *Acta Crystallogr.* **1976**, 32, 751–767.
- (22) (a) Bang, S.; Lee, Y.-M.; Hong, S.; Cho, K.-B.; Nishida, Y.; Seo, M. S.; Sarangi, R.; Fukuzumi, S.; Nam, W. Redox-inactive metal ions modulate the reactivity and oxygen release of mononuclear non-haem iron(III)—peroxo complexes. *Nat. Chem.* **2014**, *6*, 934—940. (b) Karmalkar, D. G.; Sankaralingam, M.; Seo, M. S.; Ezhov, R.; Lee, Y.-M.; Pushkar, Y. N.; Kim, W.-S.; Fukuzumi, S.; Nam, W. A High-Valent Manganese(IV)—Oxo—Cerium(IV) Complex and Its Enhanced Oxidizing Reactivity. *Angew. Chem., Int. Ed.* **2019**, *58*, 16124—16129. (c) Sankaralingam, M.; Lee, Y.-M.; Pineda-Galvan, Y.; Karmalkar, D. G.; Seo, M. S.; Jeon, S. H.; Pushkar, Y.; Fukuzumi, S.; Nam, W. Redox Reactivity of a Mononuclear Manganese-Oxo Complex Binding Calcium Ion and Other Redox-Inactive Metal Ions. *J. Am. Chem. Soc.* **2019**, *141*, 1324—1336.
- (23) Van Staveren, C. J.; Van Eerden, J.; Van Veggel, F. C. J. M.; Harkema, S.; Reinhoudt, D. N. Cocomplexation of neutral guests and electrophilic metal cations in synthetic macrocyclic hosts. *J. Am. Chem. Soc.* **1988**, *110*, 4994–5008.
- (24) Van Veggel, F. C. J. M.; Harkema, S.; Bos, M.; Verboom, W.; Van Staveren, C. J.; Gerritsma, G. J.; Reinhoudt, D. N. Metallomacrocycles: synthesis, x-ray structure, electrochemistry, and ESR spectroscopy of mononuclear and heterodinuclear complexes. *Inorg. Chem.* 1989, 28, 1133–1148.
- (25) Beesley, R. M.; Ingold, C. K.; Thorpe, J. F. CXIX.—The formation and stability of spiro-compounds. Part I. spiro-Compounds from cyclohexane. *J. Chem. Soc. Trans.* 1915, 107, 1080–1106.
- (26) Groom, C. R.; Bruno, I. J.; Lightfoot, M. P.; Ward, S. C. The Cambridge Structural Database. *Acta Cryst. B* **2016**, *72*, 171–179.
- (27) Bag, B.; Mondal, N.; Rosair, G.; Mitra, S. CCDC 151498: Experimental Crystal Structure Determination, 2001. (b) Bag, B.; Mondal, N.; Mitra, S.; Rosair, G. The First Thermally-stable Singly Oxo-bridged Dinuclear Ni(III) Complex. Chem. Commun. 2000, 1729–1730.

- (28) Zhou, H.; Pan, Z.-Q.; Zhang, Y.-J. *CCDC 625054: Experimental Crystal Structure Determination*, 2006. (b) Zhou, H.; Pan, Z.-Q.; Zhang, Y.-J. Acetato[ $\mu$  –10,21-dibutyl-3,6,14,17-tetrazatricyclo-[17.3.1.18,12]tetracosa-1(23),2,6,8,10,12(24),13,17,19,21-decaene-23,24-diolato(2-  $\kappa$ 4N<sub>3</sub>,N6,O23,O24:  $\kappa$  4N14,N17,O23,O24]dinickel-(II) perchlorate acetonitrile hemisolvate. *Acta Cryst. E* **2006**, *62*, m2442–m2444.
- (29) Wu, J.-C.; Li, Y.-Z.; Tang, N.; Tan, M.-Y. *CCDC 217382: Experimental Crystal Structure Determination*, 2003. (b) Wu, J.-C.; Li, Y.-Z.; Tang, N.; Tan, M.-Y.  $[\mu -10,21\text{-Di-tert-butyl-4}(S),5(S),15(S),16(S)\text{-tetraphenyl-3,6,14,17-tetraazatricyclo}[17.3.1.18,12]\text{-tetracosa-1}(23),2,6,8,10,12(24),13,17,19,21-decaene-23,24-diolato}](\mu -ethylene glycol)dinickel(II) diperchlorate dihydrate.$ *Acta Cryst. E***2003**,*59*, m494–m496.
- (30) Ding, Y.; Ku, Z.; Wang, L.; Hu, Y.; Zhou, Y. CCDC 654305: Experimental Crystal Structure Determination, 2008. (b) Ding, Y.; Ku, Z.; Wang, L.; Hu, Y.; Zhou, Y. Bis{μ-2,2'-[ethane-1,2-diylbis-(nitrilomethylidyne)]diphenolato}dinickel(II). Acta Cryst. E 2008, 64, m173. (c) Ding, Y.; Wang, F.; Ku, Z. J.; Wang, L. S.; Wang, Q. R. Solvent directed templated synthesis of mono- and di(Schiff base) complexes of Ni(II). Russ. J. Coord. Chem. 2009, 35, 360–366.
- (31) Tang, C. CCDC 722825: Experimental Crystal Structure Determination, 2009. Wu, Q.; Tang, Y.-F.; Zi, Q.-L. CCDC 1892682: Experimental Crystal Structure Determination, 2019.
- (32) Yang, L.; Powell, D. R.; Houser, R. P. Structural variation in copper(I) complexes with pyridylmethylamide ligands: structural analysis with a new four-coordinate geometry index,  $\tau^4$ . *Dalton Trans.* **2007**, 955–964.
- (33) Lever, A. B. P. Inorganic Electronic Spectroscopy, 2nd ed.; Elsevier Science Publishers, 1984.
- (34) Kelsey, S. R.; Kumar, A.; Oliver, A. G.; Day, V. W.; Blakemore, J. D. Promotion and Tuning of the Electrochemical Reduction of Hetero- and Homobimetallic Zinc Complexes. *ChemElectroChem* **2021**, *8*, 2792–2802.
- (35) (a) Ballhausen, C. J.; Gray, H. B. The Electronic Structure of the Vanadyl Ion. *Inorg. Chem.* **1962**, *1*, 111–122. (b) Stoklosa, H. J.; Wasson, J. R.; McCormick, J. Electronic structure of bis(2-methyl-8-quinolinolato)oxovanadium(IV). *Inorg. Chem.* **1974**, *13*, 592–597. (c) Kuska, H. A.; Yang, P.-H. Effects of substituents on the spectroscopic properties of tetradentate ligand-oxovanadium(IV) complexes. *Inorg. Chem.* **1977**, *16*, 1938–1941. (d) Garribba, E.; Micera, G.; Panzanelli, A.; Sanna, D. Electronic Structure of Oxovanadium(IV) Complexes of  $\alpha$ -Hydroxycarboxylic Acids. *Inorg. Chem.* **2003**, *42*, 3981–3987.
- (36) Isse, A. A.; Gennaro, A.; Vianello, E. A study of the electrochemical reduction mechanism of Ni(salophen) in DMF. *Electrochim. Acta* **1992**, *37*, 113–118.
- (37) (a) Gosden, C.; Healy, K. P.; Pletcher, D. Reaction of electrogenerated square-planar nickel(I) complexes with alkyl halides. *J. Chem. Soc., Dalton Trans.* **1978**, 972–976. (b) Duñach, E.; Esteves, A. P.; Medeiros, M. J.; Pletcher, D.; Olivero, S. The Study of Nickel(II) and Cobalt(II) Complexes with a Chiral Salen Derivative as Catalysts for the Electrochemical Cyclisation of Unsaturated 2-bromophenyl Ethers. *J. Electroanal. Chem.* **2004**, *566*, 39–45.
- (38) Dopp, C. M. Using Vanadyl and Its Terminal Oxo to Probe Ligand Donor Strength in Heterobimetallic Complexes. Undergraduate Thesis, University of Kansas, 2023. http://hdl.handle.net/1808/34384.
- (39) Bard, A. J.; Faulkner, L. R. Electrochemical Methods: Fundamentals and Applications; John Wiley and Sons, Inc., 1980.
- (40) Hopkins Leseberg, J. A.; Gompa, T. P.; Oliver, A. G.; Day, V. W.; La Pierre, H. S.; Blakemore, J. D. Rational Tuning of Cerium Redox Chemistry with Mono- and Divalent Redox-Inactive Metal Cations; BroadcastMed, Inc., 2023.
- (41) Savéant, J.-M.; Costentin, C. Elements of Molecular and Biomolecular Electrochemistry, 2nd; Wiley, 2019.
- (42) Connelly, N. G.; Geiger, W. E. Chemical Redox Agents for Organometallic Chemistry. *Chem. Rev.* **1996**, *96*, 877–910.

- (43) (a) Miedaner, A.; Haltiwanger, R. C.; DuBois, D. L. Relationship between the bite size of diphosphine ligands and tetrahedral distortions of "square-planar" nickel(II) complexes: stabilization of nickel(I) and palladium(I) complexes using diphosphine ligands with large bites. *Inorg. Chem.* 1991, 30, 417–427. (b) Gomes, L.; Pereira, E.; de Castro, B. Nickel(II) complexes with N<sub>2</sub>OS and N<sub>2</sub>S<sub>2</sub> co-ordination spheres: reduction and spectroscopic study of the corresponding Ni(I) complexes. *J. Chem. Soc., Dalton Trans.* 2000, 1373–1379.
- (44) Stoll, S.; Schweiger, A. EasySpin, a comprehensive software package for spectral simulation and analysis in EPR. *J. Magn. Reason.* **2006**, *178*, 42–55.
- (45) (a) Hathaway, B. J.; Billing, D. E. The electronic properties and stereochemistry of mono-nuclear complexes of the copper(II) ion. Coord. Chem. Rev. 1970, 5, 143—207. (b) Hathaway, B. J.; Tomlinson, A. A. G. Copper(II) ammonia complexes. Coord. Chem. Rev. 1970, 5, 1—43. (c) Scholl, H. J.; Huettermann, J. ESR and ENDOR of copper(II) complexes with nitrogen donors: probing parameters for prosthetic group modeling of superoxide dismutase. J. Phys. Chem. 1992, 96, 9684—9691. (d) Randall, D. W.; George, S. D.; Hedman, B.; Hodgson, K. O.; Fujisawa, K.; Solomon, E. I. Spectroscopic and Electronic Structural Studies of Blue Copper Model Complexes. 1. Perturbation of the Thiolate—Cu Bond. J. Am. Chem. Soc. 2000, 122, 11620—11631.
- (46) Nicholson, R. S. Theory and Application of Cyclic Voltammetry for Measurement of Electrode Reaction Kinetics. *Anal. Chem.* **1965**, 37, 1351–1355.
- (47) (a) Marcus, R. A. Chemical and Electrochemical Electron-Transfer Theory. *Annu. Rev. Phys. Chem.* **1964**, *15*, 155–196. (b) Marcus, R. A. On the Theory of Electron-Transfer Reactions. VI. Unified Treatment for Homogeneous and Electrode Reactions. *J. Chem. Phys.* **1965**, *43*, 679–701.
- (48) Hush, N. S. Adiabatic theory of outer sphere electron-transfer reactions in solution. *Trans. Faraday Soc.* **1961**, *57*, 557–580.
- (49) Brunschwig, B. S.; Logan, J.; Newton, M. D.; Sutin, N. A Semiclassical Treatment of Electron-exchange Reactions. Application to the Hexaaquoiron(II)-hexaaquoiron(III) System. *J. Am. Chem. Soc.* 1980, 102, 5798–5809.
- (50) Marcus, R. A.; Sutin, N. Electron transfers in chemistry and biology. *Biochim. Biophys. Acta, Rev. Bioenerg.* 1985, 811, 265-322.
- (51) Zhang, X.; Yang, H.; Bard, A. J. Variation of the heterogeneous electron-transfer rate constant with solution viscosity: reduction of aqueous solutions of [(EDTA)chromium(III)]<sup>-</sup> at a mercury electrode. J. Am. Chem. Soc. 1987, 109, 1916–1920.
- (52) Brunschwig, B. S.; Creutz, C.; Macartney, D. H.; Sham, T. K.; Sutin, N. The Role of Inner-sphere Configuration Changes in Electron-exchange Reactions of Metal Complexes. *Faraday Discuss. Chem. Soc.* **1982**, 74, 113–127.
- (53) Bangle, R. E.; Schneider, J.; Piechota, E. J.; Troian-Gautier, L.; Meyer, G. J. Electron Transfer Reorganization Energies in the Electrode–Electrolyte Double Layer. J. Am. Chem. Soc. 2020, 142, 674–679.
- (54) (a) Sutin, N. Nuclear, electronic, and frequency factors in electron transfer reactions. *Acc. Chem. Res.* **1982**, *15*, 275–282. (b) Liu, Y.-P.; Newton, M. D. Reorganization Energy for Electron Transfer at Film-Modified Electrode Surfaces: A Dielectric Continuum Model. *J. Phys. Chem.* **1994**, *98*, 7162–7169. (c) Ghosh, S.; Horvath, S.; Soudackov, A. V.; Hammes-Schiffer, S. Electrochemical Solvent Reorganization Energies in the Framework of the Polarizable Continuum Model. *J. Chem. Theory Comput.* **2014**, *10*, 2091–2102. (d) Spitler, M. T. Effect of nanometer-sized surface morphology upon electrochemical kinetics. *Electrochim. Acta* **2007**, *52*, 2294–2301.
- (55) Falivene, L.; Credendino, R.; Poater, A.; Petta, A.; Serra, L.; Oliva, R.; Scarano, V.; Cavallo, L. SambVca 2. A Web Tool for Analyzing Catalytic Pockets with Topographic Steric Maps. *Organometallics* **2016**, *35*, 2286–2293.
- (56) (a) Poater, A.; Ragone, F.; Giudice, S.; Costabile, C.; Dorta, R.; Nolan, S. P.; Cavallo, L. Thermodynamics of N-Heterocyclic Carbene Dimerization: The Balance of Sterics and Electronics. *Organometallics*

- 2008, 27, 2679–2681. (b) Poater, A.; Ragone, F.; Mariz, R.; Dorta, R.; Cavallo, L. Comparing the Enantioselective Power of Steric and Electrostatic Effects in Transition-Metal-Catalyzed Asymmetric Synthesis. *Chem.—Eur. J.* 2010, 16, 14348–14353. (c) Falivene, L.; Cao, Z.; Petta, A.; Serra, L.; Poater, A.; Oliva, R.; Scarano, V.; Cavallo, L. Towards the online computer-aided design of catalytic pockets. *Nat. Chem.* 2019, 11, 872–879.
- (57) Closs, G. L.; Miller, J. R. Intramolecular Long-Distance Electron Transfer in Organic Molecules. *Science* **1988**, 240, 440–447. (58) Creutz, C.; Sutin, N. Vestiges of the "Inverted Region" for Highly Exergonic Electron-transfer Reactions. *J. Am. Chem. Soc.* **1977**, 99, 241–243.
- (59) Amashukeli, X.; Winkler, J. R.; Gray, H. B.; Gruhn, N. E.; Lichtenberger, D. L. Electron-Transfer Reorganization Energies of Isolated Organic Molecules. *J. Phys. Chem. A* **2002**, *106*, 7593–7598.
- (60) Wenger, O. S.; Leigh, B. S.; Villahermosa, R. M.; Gray, H. B.; Winkler, J. R. Electron Tunneling Through Organic Molecules in Frozen Glasses. *Science* **2005**, *307*, 99–102.
- (61) Xiong, S.; Hong, A.; Bailey, B. C.; Spinney, H. A.; Senecal, T. D.; Bailey, H.; Agapie, T. Highly Active and Thermally Robust Nickel Enolate Catalysts for the Synthesis of Ethylene-Acrylate Copolymers. *Angew. Chem., Int. Ed.* **2022**, *61*, No. e202206637.
- (62) Wu, K.; Doyle, A. G. Parameterization of phosphine ligands demonstrates enhancement of nickel catalysis via remote steric effects. *Nat. Chem.* **2017**, *9*, 779–784.
- (63) Fukuzumi, S.; Ohkubo, K.; Lee, Y.-M.; Nam, W. Lewis Acid Coupled Electron Transfer of Metal—Oxygen Intermediates. *Chem.—Eur. J.* **2015**, *21*, 17548–17559.
- (64) (a) Oswald, V. F.; Lee, J. L.; Biswas, S.; Weitz, A. C.; Mittra, K.; Fan, R.; Li, J.; Zhao, J.; Hu, M. Y.; Alp, E. E.; et al. Effects of Noncovalent Interactions on High-Spin Fe(IV)—Oxido Complexes. J. Am. Chem. Soc. 2020, 142, 11804—11817. (b) Prat, J. R.; Gaggioli, C. A.; Cammarota, R. C.; Bill, E.; Gagliardi, L.; Lu, C. C. Bioinspired Nickel Complexes Supported by an Iron Metalloligand. Inorg. Chem. 2020, 59, 14251—14262.
- (65) (a) Krivovichev, S. V.; Cahill, C. L.; Burns, P. C. Syntheses and Crystal Structures of Two Topologically Related Modifications of Cs<sub>2</sub>[(UO<sub>2</sub>)<sub>2</sub>(MoO<sub>4</sub>)<sub>3</sub>]. *Inorg. Chem.* **2002**, *41*, 34–39. (b) Frisch, M.; Cahill, C. L. Syntheses, structures and fluorescent properties of two novel coordination polymers in the U-Cu-H<sub>3</sub>pdc system. *Dalton Trans.* **2005**, 1518–1523. (c) Cahill, C. L.; de Lill, D. T.; Frisch, M. Homo- and heterometallic coordination polymers from the f elements. *CrystEngComm* **2007**, *9*, 15–26.
- (66) Arnold, P. L.; Patel, D.; Wilson, C.; Love, J. B. Reduction and selective oxo group silylation of the uranyl dication. *Nature* **2008**, *451*, 315–317.
- (67) Karnes, J.; Kumar, A.; Hopkins Leseberg, J.; Day, V.; Blakemore, J. Trivalent Cations Slow Electron Transfer to Macrocyclic Heterobimetallic Complexes. *ChemRxiv* **2024**.